TEL AVIV UNIVERSITY

The Iby and Aladar Fleischman Faculty of Engineering

The Zandman-Slaner School of Graduate Studies

A Time-Domain Computational Framework for Ultra-Short Pulse Beam Shaping in Ultrasound Imaging

A thesis submitted toward the degree of
Master of Science in Electrical Engineering

by

Oz Shaul Shaul

This research was carried out in the School of Electrical Engineering
Under the supervision of Prof. Tali Ilovitsh

May 25

TEL AVIV UNIVERSITY

The Iby and Aladar Fleischman Faculty of Engineering

The Zandman-Slaner School of Graduate Studies

A Time-Domain Computational Framework for Ultra-Short Pulse Beam Shaping in Ultrasound Imaging

A thesis submitted toward the degree of

Master of Science in Electrical Engineering

by

Oz Shaul Shaul

This research was carried out in the School of Electrical Engineering

Under the supervision of Prof. Tali Ilovitsh

Acknowledgments

I would like to express my deepest gratitude to my supervisor, Prof. Tali Ilovitsh, for her invaluable support, guidance, and confidence in me throughout this work. Her insight, encouragement, and patience were instrumental in shaping this research and bringing it to completion.

I also wish to thank the members of our lab for their collaboration, technical assistance, and thought-provoking discussions.

Finally, I am grateful to my family and my spouse for their constant encouragement, understanding, and emotional support during the more challenging stages of this journey.

Abstract

Beam shaping for ultra-short pulses is a critical challenge across various wave-based technologies, where precise control of wavefronts is required to optimize energy distribution and achieve desired spatial patterns. Conventional beam shaping methods, such as the widely used Gerchberg–Saxton (GS) algorithm, are inherently designed for continuous-wave excitation and are thus poorly suited for ultra-short pulse applications, particularly single-cycle pulses that are essential for precision control in wave-based systems. These phase-based techniques often suffer from phase ambiguity, signal degradation, and temporal distortion when applied to pulsed regimes, limiting their effectiveness in both simulations and real-world use.

This study addresses this challenge by introducing a Spatio-Temporal Adaptive Reconstruction (STAR) algorithm, designed to operate directly in the time domain, combined with a generalized Angular Spectrum Method (GASM) to accurately model the transient dynamics of short pulses. While the method is broadly applicable to fields such as optics, acoustics, and radars, its capabilities are demonstrated within the context of medical ultrasound. Here, the STAR algorithm enables precise beam shaping for single-cycle and multi-foci patterns, overcoming the limitations of conventional algorithms like the GS method and deep learning-based approaches. This framework achieves enhanced resolution, improved energy distribution, and greater adaptability to varying depths and frequencies, as validated through simulations and experimental measurements. The results highlight its potential for integration into real-time systems, paving the way for advancements in ultrasound imaging and other wave-focused applications.

Contents

Abbreviations and symbols

A-mode	Amplitude mode
B-mode	Brightness mode
CW	Continuous Wave
GS	Gerchberg-Saxton
MI	Mechanical Index
SNR	Signal to Noise Ration
US	Ultrasound
λ	Wavelength
ASM	Angular Spectrum Method
GASM	Generalized ASM
d	Aperture width
f	Frequency
v [$\frac{m}{sec^2}$]	Speed of sound
z [mm]	Depth
φ	Phase
PNP	Peak Negative Pressure
STAR	Spatio Temporal Adaptive Reconstruction
CNN	convolutional neural networks
HIFU	High-Intensity Focused Ultrasound
GAN	Generative adversarial networks

List of figures

List of Publications

Journal papers:

1. **O. Shaul**, T. Ilovitsh, "Spatio-Temporal Adaptive reconstruction", (Under Review in Physical Review X, 2025).
2. B. Glickstein, M. Bismuth, R. Gattegno, T. Bercovici, **O. Shaul**, R. Aronovich, G. Horn, A. G. Levin, Y. Feng, T. Ilovitsh, "Volumetric Nanodroplet-Enhanced Ultrasound Surgery Combined with Immune Checkpoint Inhibition as a Cancer Therapy Platform", Small, 2025.
3. B. Glickstein, **O. Shaul** and T. Ilovitsh, "Rationally Designed Acoustic Holograms for Uniform Nanodroplet-Mediated Tissue Ablation," IEEE Transactions on Ultrasonics, Ferroelectrics, and Frequency Control, vol. 71, no. 11, pp. 1606-1615, Nov. 2024.

1 Introduction

Wavefront shaping is a fundamental concept in various wave-based technologies, including optics, acoustics, microwaves, and biomedical imaging. It enables precise control over the spatial and temporal properties of waves, allowing tailored energy distribution for specific applications. Applications such as high-resolution imaging [1], optical trapping [2],[3], focused energy delivery [4] and acoustic holography [5] rely on the ability to manipulate wavefronts to achieve desired field distributions. Various methods have been developed to accomplish this, ranging from iterative phase-retrieval algorithms to optimization-based techniques and, more recently, deep learning-driven approaches.

One of the most established classes of wavefront shaping techniques is iterative phase-retrieval methods, where an initial wavefront is iteratively refined to match a target intensity distribution. The GS algorithm [6], one of the most popular methods in this category, alternates between the transducer plane and the focal plane, enforcing constraints in each domain to converge toward the desired beam profile. Variants of the GS algorithm, such as the adaptive weighted gs algorithm [7], the optimized adaptive weighted GS algorithm [8] and the modified GS algorithm [9] introduce refinements to enhance accuracy, convergence speed and robustness.

Another widely used category is optimization-based wavefront shaping, where numerical techniques, such as gradient descent [10], genetic algorithms [11] and automatic differentiation [12] are employed to iteratively refine the input wavefront. These methods offer higher accuracy but are often computationally expensive, limiting their applicability in real-time settings.

More recently, deep learning-based approaches have been explored for wavefront shaping. These include convolutional neural networks (CNNs) [13],[14],[15], autoencoder frameworks [16],[17], and generative adversarial networks (GANs) [18], which enable direct mapping between input and desired wavefronts. These methods have demonstrated improved performance in complex scenarios but often require large training datasets and lack interpretability.

Among these approaches, the GS algorithm remains widely used due to its simplicity, rapid convergence and flexibility in optimizing different parameters such as frequency and depth. However, while effective for continuous-wave (CW) signals, the GS algorithm, as well as other methods, struggles with ultra-short pulses, particularly single or two-cycle pulses. This limitation stems from the reliance on wave propagation models which assume steady-state or CW insonation, such as the Angular Spectrum Method (ASM).

To overcome these limitations, we propose the STAR algorithm that enables direct time-domain optimization for precise wavefront shaping of ultra-short pulses.

Ultra-short pulses are critical across multiple fields, as they enable improved resolution, enhanced energy delivery, and reduced interference. In radar and wireless communications, ultra-short pulses provide better resolution, precise distance measurement, improved target recognition, enhanced resistance to noise and interference, and reduced detectability [19]. In optical microscopy and super-resolution imaging, techniques such as two-photon fluorescence microscopy [20] and stimulated emission depletion (STED) [21] microscopy rely on ultra-short laser pulses to achieve deeper penetration depths and sub-diffraction-limited resolution.

In medical ultrasound imaging, a widely used imaging modality in healthcare, ultra-short pulses play a crucial role in achieving high axial resolution, enabling the distinction of closely spaced anatomical structures while minimizing tissue heating and bioeffects [22]. Ultrasound imaging is applied in diagnostic procedures, including pregnancy monitoring [23], cardiology [24], and oncology [25], as well as in therapeutic interventions such as focused ultrasound surgery [26] and targeted drug delivery [27].

To address the need for wavefront shaping with ultra-short pulses, a deep convolutional residual network-based approach was developed in [28] for beam shaping with single-cycle excitation. This study demonstrated superior performance compared to the GS algorithm in terms of accuracy and computational efficiency. However, its applicability is limited by the frequency and depth range of the training dataset, limiting generalization.

This study aims to develop a wavefront shaping algorithm that retains the adaptability of the GS algorithm while enabling robust performance for ultra-short pulses, including single-cycle excitations and other transient signal types.

A key technique for modeling wave propagation in ultrasound and other wave-based applications is the ASM [29], which models wavefields by decomposing them into plane waves with distinct propagation directions and amplitudes. Initially designed for CW signals, ASM has been instrumental in ultrasound applications due to its computational efficiency and accuracy, making it a core component of the GS algorithm as well. However, the conventional ASM struggles with short pulses due to its inherent reliance on steady-state, harmonic solutions [30]. The broadband, transient nature of short pulses necessitates a generalized approach to adequately capture their propagation dynamics. To address this limitation, the ASM has been extended to accommodate pulsed ultrasound signals, leveraging a time-domain framework to account for the transient nature of these signals [31]. This generalized method, GASM, provides a robust foundation for modeling the propagation of short pulses, enabling accurate simulation of acoustic fields for advanced imaging applications.

Here, we propose the STAR algorithm to beam shape the acoustical field, and operates directly in the time domain. By integrating the GASM into the GS framework, the STAR algorithm overcomes the constraints of phase-domain optimization, allowing for precise wavefront shaping of ultra-short pulses. Chapter 2 outlines the main research objectives and motivations. Chapter 3 provides the theoretical background, including medical ultrasound principles, ultrasound wave propagation, beam shaping in the field of ultrasound and the challenges dealing with ultra-short pulses. Chapter 4 details the methodology, including the GASM, the STAR algorithm, the simulation framework, and the experimental setup used for validation. Chapter 5 presents the simulation results and experimental measurements obtained using hydrophone scans. Finally, Chapter 6 discusses the implications, potential applications, and limitations of the proposed approach, and concludes with directions for future research. Chapter 7 provide a conclusion for this study.

2 Research objectives

The objective of this research is to develop and validate a time-domain beam shaping algorithm, STAR, capable of controlling the spatiotemporal distribution of ultra-short wave pulses, including single-cycle excitations. We aim to implement and demonstrate it in the context of ultrasound. The study proceeds in the following steps:

(1) Implementation of a GASM to accurately model the transient propagation of single-cycle pulses

(2) Validation of the GASM performance using a numerical simulation tool (k-Wave) under relevant pulse conditions

(3) Formulation of the STAR algorithm to perform spatiotemporal phase retrieval directly in the time domain

(4) Integration of the GASM within the STAR framework and its full implementation

(5) Implementation of the GS algorithm as a benchmark for comparison

(6) Experimental evaluation of the proposed method using hydrophone measurements to validate beam shaping performance.

The final framework aims to advance spatiotemporal control of pulsed wavefronts in ultrasound imaging, improving resolution, energy focus, and multi-foci patterning.

3 Theoretical Background

3.1 Medical Ultrasound principles

3.1.1 Ultrasound Wave Generation and Propagation

Ultrasound refers to mechanical sound waves with frequencies above the range of human hearing (greater than 20 kHz). Diagnostic medical ultrasound typically operates in the low megahertz range (roughly 1–15 MHz) [32]. These ultrasound waves are longitudinal pressure waves that propagate through tissue as alternating compressions and rarefactions of the medium. The propagation speed of sound in a medium depends on its properties, in soft biological tissues the average sound speed is about 1540 m/s [33]. As with any wave, wavelength and frequency are related by the wave speed, so higher-frequency ultrasound has a shorter wavelength. For example, a 5 MHz ultrasound wave in soft tissue has a wavelength on the order of 0.3 mm. This small wavelength is what enables ultrasound imaging to resolve fine anatomical details, but the high frequency also affects how far the wave can penetrate, as discussed later.

Medical ultrasound systems generate and detect ultrasound pulses using pulse-echo. A short electrical excitation is applied to a piezoelectric transducer which converts it into a brief acoustic pulse that travels into the body. As the ultrasound pulse propagates, it encounters boundaries and tissues of differing properties that partially reflect the wave. The transducer then switches to listening mode to detect returning echoes, converting the mechanical pressure of each echo back into an electrical signal. By measuring the round-trip travel time of echoes, the system can determine the depth of the reflecting structure. Successive pulse-echo cycles are repeated hundreds or thousands of times per second to produce a real-time image. In summary, an ultrasound image is built from the time delays and amplitudes of many echoes returning from structures in the body.

3.1.2 Resolution and tradeoffs in Ultrasound Imaging

Ultrasound imaging performance is intrinsically linked to the frequency of the waves used. There is a fundamental trade-off between spatial resolution and penetration depth that the operator or system must balance [34]. Higher ultrasound frequencies yield better spatial resolution (ability to distinguish small or closely spaced structures) because of their shorter wavelength. However, high frequencies are also attenuated more rapidly in tissue, which reduces the penetration depth. Lower frequencies penetrate farther into the body but have longer wavelengths, which degrade resolution. This inverse relationship means that no single frequency is optimal for all situations, and the choice of transducer frequency is a critical decision in ultrasound imaging.

The improvement in resolution with frequency can be understood qualitatively by considering axial resolution and lateral resolution. Axial resolution (along the beam direction) is determined by the spatial pulse length – proportional to the wavelength and the number of cycles in the pulse.

$$\Delta z_{axial} \geq N_c \cdot \frac{\lambda}{2} \tag{1}$$

where N_c is the number of cycles in the pulse and λ is the wavelength.

Using low number of cycles or higher frequency directly reduces the spatial pulse length, thus yielding finer axial resolution. For instance, a typical diagnostic pulse at 10 MHz might have an axial resolution on the order of 0.1 mm, whereas at 1 MHz it might be ~1 mm. Lateral resolution is the smallest distance between two objects lying in the lateral direction (perpendicular to wave propagation direction), that can be detected. This lateral resolution is determined by the diffraction limitation. For plane-wave imaging, with a rectangular aperture the lateral resolution is defined by:

$$\Delta x_{lateral} \geq 1.206 \cdot \frac{\lambda \cdot z}{d} \tag{2}$$

where d is the aperture width, and z is the distance between the transducer and the object.

With higher frequency, a given aperture size can produce a narrower beam, and transducer arrays can more tightly focus the beam, improving lateral resolution. In effect, high-frequency ultrasound produces sharper, more detailed images. The penalty for high frequency is limited depth penetration due to frequency-dependent attenuation. Acoustic attenuation in soft tissue increases approximately linearly with frequency in the diagnostic range. Thus a 10 MHz beam loses energy much faster than a 1 MHz beam as it travels. At a certain depth, the echoes from a high-frequency probe may become too weak to detect.

3.1.3 Imaging modes in Ultrasound

Ultrasound imaging systems employ various operational modes to capture and display diagnostic information, each mode offering different insights into anatomical and physiological properties

[36]. The most basic is A-mode (Amplitude Mode), which presents a one-dimensional representation of echo amplitude as a function of depth. Although now largely obsolete for most clinical applications, A-mode remains in use for precise distance measurements in ophthalmology. In contrast, B-mode (Brightness Mode) is the standard imaging modality in diagnostic ultrasound. It provides real-time two-dimensional grayscale images by mapping the amplitude of backscattered echoes to pixel brightness, based on their depth and lateral position. Each vertical scan line is generated from a pulse-echo sequence, and a full image is assembled by sweeping the beam across the region of interest. B-mode imaging is foundational in nearly all modern ultrasound applications, from abdominal to obstetric and musculoskeletal imaging. Doppler modes extend ultrasound’s capabilities by measuring the velocity and direction of moving targets, typically blood cells. Continuous-wave Doppler detects high-velocity flows but lacks depth resolution, while pulsed-wave Doppler offers range-specific flow assessment but is limited by aliasing at higher velocities [37].

3.1.4 Therapeutic Ultrasound Applications

In addition to its diagnostic role, ultrasound serves as a therapeutic modality in several medical contexts [38]. High-Intensity Focused Ultrasound (HIFU) is used for non-invasive tissue ablation, such as in prostate or liver tumors, by concentrating acoustic energy to induce localized heating. Low-intensity ultrasound is applied in physiotherapy to promote tissue healing and reduce inflammation. Emerging applications include ultrasound-mediated drug delivery, cellular sonication, and gene therapy, often enhanced by microbubble contrast agents [39]. Unlike diagnostic ultrasound, therapeutic systems operate at significantly higher intensities and require precise targeting to achieve biological effects safely. In both diagnostic and therapeutic contexts, precise control over the ultrasound beam is crucial and fundamentally linked to the shape of the wavefront. In recent years, algorithms like GS have been employed not only for focusing in imaging but also in therapeutic applications. Notably, 3D-printed acoustic holograms designed using GS have been demonstrated and can serve roles in both imaging and therapy [40]

3.2 The Angular Spectrum Method

The ASM is a frequency-domain technique for modeling wave propagation by decomposing a wavefield into plane waves. In a homogeneous medium, any acoustic pressure field on a plane can be represented as a superposition of plane waves (a spatial Fourier decomposition). The ASM propagates this plane-wave spectrum from one plane to another by applying phase shifts (or filters) corresponding to the propagation distance for each spatial frequency component. This method is widely used in ultrasound to efficiently simulate pressure fields produced by transducers, for example to calculate the field from an array or a focused transducer in water or tissue [41].

Mathematically, the ASM can be expressed as follows. Let the initial pressure field at the transducer surface be given by $p(x, y, z_0)$. The angular spectrum of this field is defined as the two-dimensional Fourier transform:

$$P(k_x, k_y, z) = \iint_{-\infty}^{\infty} p(x, y, z_0) e^{-j(k_x x + k_y y)} \, dx dy \tag{3}$$

where k_x and k_y are the spatial frequency components in the x and y directions, respectively, and z is the position of the given plane in the z direction

The pressure field at a plane in depth of z_1 can then be calculated as:

$$P_1(k_x, k_y, z_1) = P_0(k_x, k_y, z_0)H_p(k_x, k_y) \tag{4}$$

$$H_p(k_x, k_y) = \begin{cases} e^{-j(z_1-z_0)\sqrt{k^2-k_x^2-k_y^2}}, k^2 > k_x^2 + k_y^2 \\ e^{-(z_1-z_0)\sqrt{k^2-k_x^2-k_y^2}}, k^2 \leq k_x^2 + k_y^2 \end{cases} \tag{5}$$

where P_0 and P_1 are the angular spectrums in depths of z_0 and z_1 respectively, and k is the wavenumber, with f being the frequency and c the speed of sound in the medium

3.3 Beam Shaping

Beam shaping refers to the intentional design of the ultrasound field pattern beyond a simple single focus. In conventional ultrasound imaging, the transmitted beam is usually focused at one point or a line, but beam shaping techniques seek to control the spatial distribution of acoustic energy more elaborately. This can include sidelobe reduction, multi-focal patterns, or custom intensity profiles in the field. In array transducers, beam shaping is achieved by manipulating the phase and amplitude (apodization) of each element's excitation. By adjusting these degrees of freedom, one can synthesize a desired interference pattern in the medium. Unlike a fixed acoustic lens or curved transducer (which provides one static focus), electronic beam shaping is dynamic and configurable in real-time. Common beam shaping approaches in conventional systems include apodization windows (e.g. Hanning or Gaussian weighting to reduce sidelobes at the cost of a wider main lobe). In therapeutic ultrasound (e.g. hyperthermia for example, where continuous-wave or long bursts are used, advanced beam shaping has been deployed to create multiple foci or uniform sonication regions. These continuous-wave beam shaping methods can rely on steady-state interference and often assume a single frequency for simplicity. Well-established algorithms for beam shaping include the conjugate field method (using the phase-conjugate of the field from target to array), and pseudo-inverse methods that mathematically invert the propagation to solve for the required source distribution. More recently, deep learning techniques have also been introduced into this domain. Each method presents trade-offs between computational complexity, accuracy, and robustness. Among these methods, the GS algorithm is particularly popular in the field of ultrasound, as it offers high efficiency and produces focal spots with good uniformity [42].

3.4 The Gerchberg-Saxton Algorithm

The GS algorithm is an iterative phase retrieval method originally developed for optics, which has been adapted to acoustics for tasks such as beam shaping and holographic focusing. The algorithm aims to find a complex wavefield (with both amplitude and phase) that satisfies constraints in two domains (typically two parallel planes). In the context of ultrasound, one plane might be the transducer surface and the other the target focal plane.

The GS algorithm can be summarized as follows (Fig 1.): First, the phase distribution across the transducer elements is initialized to be uniform. Next, the initial pressure field is propagated to the focal plane using the ASM, with the target depth set to 40 mm. At the focal plane, the desired amplitude constraint is applied while preserving the phase information. Subsequently, inverse propagation is calculated to obtain the updated pressure field in the transducer plane. An amplitude constraint is then applied in the transducer plane by setting the amplitude to 1 for x values within the transducer's region and 0 for those outside it. These steps are repeated iteratively until the algorithm converges to the desired beam profile.

After the final iteration of the GS algorithm, the resulting phase distribution across the transducer elements is unwrapped. The motivation for this unwrapping step is to remove any discontinuities in the phase and better exploit the time-domain properties of the signal. The unwrapping process involves adding or subtracting multiples of 2π to the phase values, ensuring a smooth, continuous phase function.

Then, the resulting apodization-phase distribution across the transducer elements can be used to drive the ultrasound system and generate the desired acoustic beam shape.

One major assumption in the classical GS is that we deal with a monochromatic (single-frequency) wavefield, so that we can propagate with a single-frequency model. In ultrasound adaptation, this usually means we design for a particular frequency (e.g., the center frequency of the transducer).

```
Algorithm 1 Gerchberg-Saxton Algorithm
Input: Target amplitude distribution at focal plane, target depth $z = 40\text{mm}$.
Initialize: Set initial phase distribution across transducer elements as:
    $p(x, z_0) = A_i \cdot \exp(i \cdot \phi_i) = 1.$
repeat
    Propagate the pressure field from the transducer plane to the focal plane using the Angular Spectrum approach:
        $p(x, z_1 = 40\text{mm}) = ASM\{p(x, z_0), D = z_1 - z_0\} = a_i \cdot \exp(i \cdot \Phi_i)$
    Apply the desired amplitude constraint at the focal plane while preserving the phase information.
        $a_i \cdot \exp(i \cdot \Phi_i) \rightarrow b_i \cdot \exp(i \cdot \Phi_i)$
    Compute the inverse propagation to return to the transducer plane.
        $\tilde{p}(x, z_0) = ASM\{p(x, z_1), D = z_0 - z_1\} = \tilde{A}_i \cdot \exp(i \cdot \tilde{\phi}_i)$
    Apply the amplitude constraint in the transducer plane:
        $\tilde{p}(x, z_0) = \begin{cases} \exp(i \cdot \tilde{\phi}_i), & \text{if } x \text{ is in the transducer's region,} \\ 0, & \text{otherwise.} \end{cases}$
until The algorithm converges to the desired beam profile.
Output: Phase distribution that generates the desired beam profile.
```

Figure 1. Pseudocode of the GS Algorithm

3.5 Challenges in beam shaping of ultra-short pulses

When it comes to imaging with ultra-short pulses, beam shaping faces additional constraints. Because imaging ideally uses one-cycle pulses (for best resolution), the ability to maintain a complicated spatial pattern is limited by the length of the pulse. With a continuous wave or a long pulse, any desired number of interference fringes or foci can be sustained as long as the transmission continues. In contrast, a single-cycle pulse only allows a very short interaction, reducing the dynamic range between designed focal points and background and limiting how many distinct foci can be generated simultaneously. In practical terms, if one attempts to create multiple simultaneous focal spots with a one-cycle pulse, all those foci must occur within the pulse length in time (and along the propagation path).

For example, the GS algorithm exhibits limited performance when applied to short pulses, as it relies on the ASM, which assumes narrowband signals, an assumption that breaks down in the case of high-bandwidth, short temporal pulses.

4 Materials and methods

4.1 The Generalized Angular Spectrum for Pulsed Signals

For conventional narrowband ultrasound (multi-cycle pulses or continuous wave), the ASM is often applied at the center frequency (assuming a harmonic steady-state). The field can be computed for that frequency and used as a representative solution. When dealing with broadband or ultra-short pulses, the ASM must account for the wide frequency content. One approach is to split the pulse into multiple frequency components, propagate each component via ASM, and then sum them (essentially performing an inverse Fourier transform in time). This pulsed angular spectrum approach was demonstrated by [31]. The pulsed ASM can closely match time-domain simulations or hydrophone measurements (within a few percent error). Thus, the ASM extends naturally to ultra-short pulses, but requires more computation (propagating many frequencies).

This generalization (GASM) to calculate the pressure field for multi-frequency signal is described mathematically as follows:

$$P\left(k_x, k_y, z, f\right) = \iiint_{-\infty}^{\infty} p(x, y, z, t) e^{-j2\pi f t} e^{-j(k_x x + k_y y)} dt dx dy \tag{6}$$

where now $p(x, y, z, t)$ is now dependent on time and $P\left(k_x, k_y, z, f\right)$ is the angular spectrum which is dependent also on the temporal frequency, f, as the 3D fourier transform was calculated (over x,y and t).

The relation between the angular spectrums in parallel planes (in depths of z_0 and z_1) is:

$$P_1\big(k_x, k_y, z_1, f\big) = P_0\big(k_x, k_y, z_0, f\big) H_p^f(k_x, k_y, f) \tag{7}$$

$$H_p^f\big(k_x, k_y, f\big) = \begin{cases} e^{-j(z_1 - z_0)\cdot sgn(f)\cdot\sqrt{k^2 - k_x^2 - k_y^2}}, & k^2 > k_x^2 + k_y^2 \\ e^{-(z_1 - z_0)\sqrt{k^2 - k_x^2 - k_y^2}}, & k^2 \le k_x^2 + k_y^2 \end{cases} \tag{8}$$

And finally the pressure field in depth of z_1 is given by:

$$p(x, y, z_1, t) = F_{3D}^{-1}\big\{F_{3D}\{p(x, y, z_0, t)\} H_p^f\big(k_x, k_y, f\big)\big\} \tag{9}$$

This generalized formulation allows for the accurate modeling of the propagation of short, pulsed signals in general and specifically in ultrasound imaging, as it takes into account the temporal evolution of the pressure field, in addition to the spatial distribution.

4.2 The STAR Algorithm for Pulsed Signals

The proposed STAR algorithm beam shapes the acoustic field by iteratively propagating the spatiotemporal signal waveform between the transducer plane and the focal plane using the GASM propagation function, while enforcing constraints on amplitudes, delays, and pulse duration in both spatial and temporal domains. The algorithm utilizes 1-cycle excitations for each transducer element. The STAR algorithm can be summarized as follows (steps are numbered in Fig. 2):

```
Algorithm 2 STAR Algorithm
Input: Target beam pattern at focal plane, target depth $z = 40\,\text{mm}$.
Initialize: Set signals for each element as 1-cycle pulses with zero delay and uniform apodization.
    $p(x,t,z_0) = \begin{cases} sin(2\pi f t), & \text{if } 0 < t < T, \\ 0, & \text{otherwise.} \end{cases}$
    where: $T = 1/f$
repeat
    Propagate the initial pressure field to the focal plane in the target depth using GASM method:
        $p(x,t,z_1 = 40\text{mm}) = \text{GASM}\{p(x,t,z_0),\ D\}$
        where: $D = z_1 - z_0$
    Apply amplitude constraints at the focal plane:
        $p(x,t,z_1) \rightarrow C(x)p(x,t,z_1)$
        where: $C(x)$ includes the amp. constraint
    Perform inverse propagation to return to the transducer plane:
        $\tilde{p}(x,t,z_0) = \text{GASM}\{C(x)p(x,t,z_1),\ -D\}$
    Determine the maximum peak pressure and its temporal location for each transducer element.
    Apply constraints on signal duration at the transducer plane:
        $\tilde{p}(x,\tilde{t},z_0) = \begin{cases} sin(2\pi f \tilde{t}), & \text{if } 0 < \tilde{t} < T, \\ 0, & \text{otherwise.} \end{cases}$
        where: $\tilde{t} = t - d(x)$
        $d(x)$ is the measured delay for each signal
until The algorithm converges to the desired beam pattern. Stopping criteria is described in detail in the paper.
Output: $d_i(x)$ - the temporal delay for each element determined from the selected i-th iteration.
```

Figure 2. Pseudocode of the STAR Algorithm

Signals for each transducer element are initialized as single-cycle pulses with zero delay and uniform apodization (step 2). The initial pressure field is then propagated to the focal plane at the target depth of 40 mm using the GASM (step 4). Amplitude constraints are applied in the focal plane to match the desired beam pattern, while the original signal shape and temporal delays are preserved (step 5). The updated pressure field is obtained by performing inverse propagation back to the transducer plane (step 6), where the maximum peak pressure and its temporal location for each transducer element are determined (step 7). Signal duration constraints are applied at the transducer plane, ensuring that each element's signal remains a single-cycle pulse. The temporal peak locations identified earlier are used as reference delays, and unity apodization is implemented within the transducer region to maximize transmitted energy, while the amplitude is set to zero outside this region (step 8). These steps are iteratively repeated until convergence to the desired beam pattern is achieved. The output pattern is obtained by taking the maximum peak value of the real part of each signal in the focal plane after step 4 of the algorithm. This provides the amplitude distribution across the spatial domain at the target depth. A schematic illustration of the algorithm is provided in Fig 3. Two key parameters are used to measure the success in designing the desired pattern: 1. Normalized cross-correlation between the desired pattern and the output pattern: This value should be maximized, as we want the output pattern to match the desired pattern as closely as possible. However, the maximum achievable value is 1, as the patterns cannot be identical. 2. Peaks Uniformity Coefficient: This metric quantifies the uniformity of the focal heights across the focal plane. It is calculated as the ratio of the standard deviation to the mean of the focal heights. A lower value indicates more similar peak amplitudes, which is desirable for applications like enhancing super resolution. By optimizing these two parameters through the iterative STAR algorithm, the goal is to generate an output pattern that closely matches the desired target while maintaining uniformity in the focal plane.

The algorithm's output is the temporal delays for each transducer element, determined from the selected iteration. The stopping criteria considers two conditions. First, the Peaks uniformity coefficient must be less than a defined threshold. Second, the normalized cross-correlation should not vary by more than 10% across the last 10 consecutive iterations. If these conditions are not satisfied, the algorithm terminates after 100 iterations and selects the output corresponding to the iteration with the minimum Peaks uniformity coefficient.

Unlike phase-based methods, this approach directly computes the temporal delays, eliminating the need for phase unwrapping. The resulting delay distribution across the transducer elements can then be implemented to shape the desired acoustic beam in the ultrasound system.

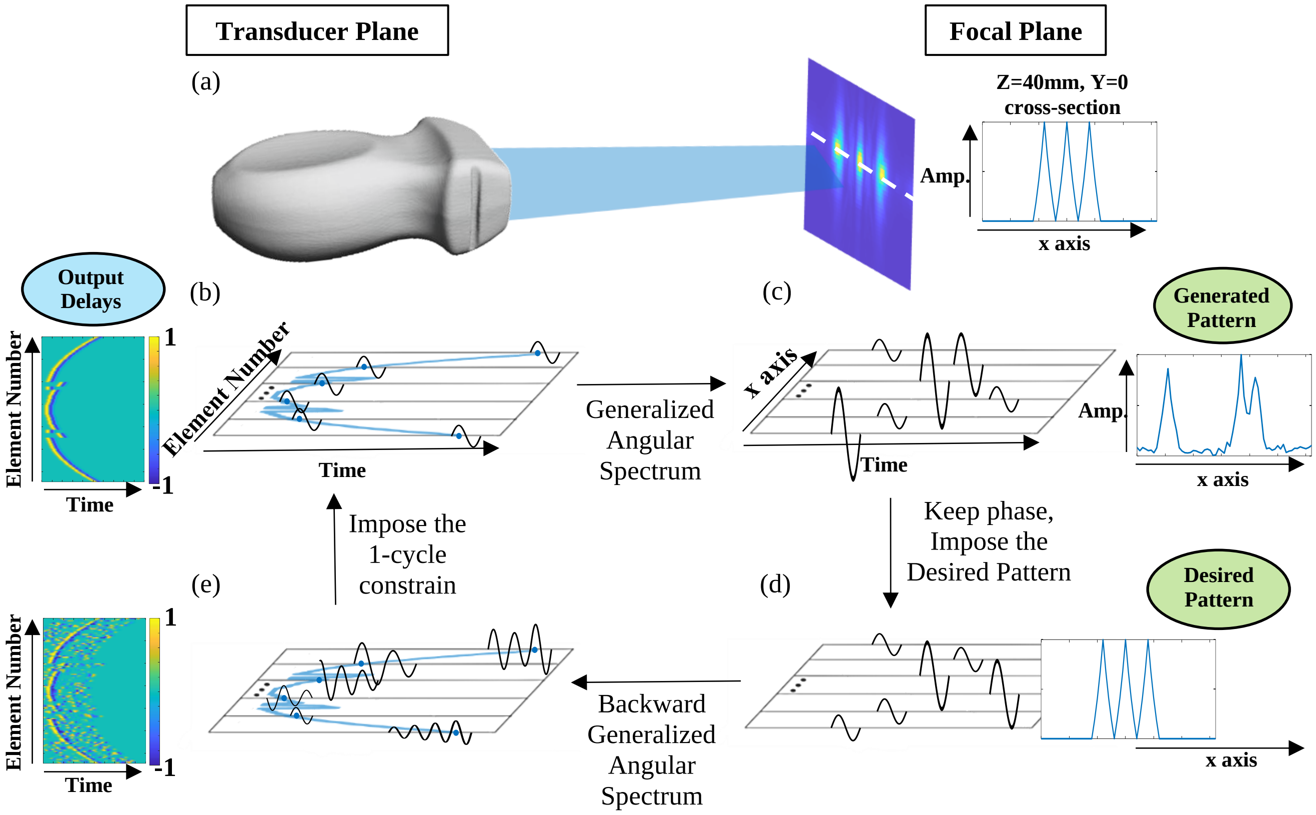

Figure 3. Schematic illustration of the STAR algorithm. (a) A schematic representation of the transducer transmitting signals, illustrating the emission of the acoustic field which propagates to the focal plane. At the focal plane, the generated acoustic pattern at the target depth is displayed along with its cross-section, providing a visual reference for the expected algorithm output. (b) Initial single-cycle signals, identical for all elements in the first iteration, are transmitted and propagated forward using the GASM. (c) the propagated signals at the focal plane exhibit varying amplitudes and delays, from which the output pattern is extracted by identifying the maximum peak pressure at each element. (d) the application of the desired pattern constraint, where delays remain unchanged while amplitudes are normalized according to the target pattern. Because the desired pattern is primarily concentrated along the center of the x-axis, elements in the middle exhibit higher amplitudes than those at the edges. (e) The signals are backward-propagated to the transducer plane, where they are no longer single-cycle. Next to this, the signals are represented as a colormap, providing a visualization of their structure. Finally (back in (b)), the transducer plane constraint is enforced — signals are truncated to single-cycle duration with uniform amplitude, and the delays are derived from the maximum peak locations, forming the final output of the algorithm.

4.3 Simulations

Both methods (ASM and GASM) were implemented in MATLAB and demonstrated by simulating signal propagation from a P6-3 transducer (Philips, Bothell, WA, USA), that was used in the experiments. The P6-3 transducer features 128 elements, a center frequency of 4.46 MHz, and a pitch of 0.22 mm.

Validation of both methods was performed through comparison with the k-Wave Simulation Tool, a robust numerical framework for modeling acoustic wave propagation. Unlike the previously discussed analytical methods, k-Wave utilizes a computational, grid-based approach to simulate the propagation of acoustic waves.

The ASM was validated against k-Wave simulations implemented in MATLAB by transmitting long pulses exceeding 10 cycles (more than 2 μs) in duration. The GASM, on the other hand, was validated using 1-cycle pulses (~0.22 μs) for a direct comparison with the proposed approach.

The toneBurst function from the k-Wave toolbox was used to generate ultrasound signals for each transducer element during implementation of both the GASM and the STAR algorithm presented subsequently.

4.4 Experimental Ultrasound setup

To validate the proposed algorithm, experimental measurements were performed using a Verasonics ultrasound system (Vantage 256, Verasonics, Kirkland, WA, USA) equipped with a P6-3 phased array transducer. The transducer was programmed to transmit signals from each individual element, with delays calculated using both the STAR and GS algorithms. The transducer emitted signals into a degassed water tank, and the resulting acoustic pressure field was measured using a needle hydrophone (NH0200, Precision Acoustics, Dorchester, U.K.) with an active aperture of 0.2 mm (FIG. 4). The hydrophone was mounted on a motorized xyz stage that was controlled by a motion controller (Newport ESP300) controller.

The pressure signals detected by the hydrophone were sampled using a digital oscilloscope (MDO3024, Tektronix, Beaverton, OR, USA) and transferred to a computer for post-processing. The post-processing included generating acoustic pressure maps for the analyzed region.

The acoustic field patterns generated by the STAR algorithm were compared to those obtained from simulations as well as to patterns produced using the GS algorithm. For a fair comparison, the transmitted signals for both algorithms were set to a duration of one cycle, consistent with the parameters used in the STAR.

Peak Negative Pressure (PNP) was determined from the measured voltage signal. The PNP at each focus reached up to 0.54 MPa, corresponding to a maximum mechanical index (MI) of 0.25. Notably, as the number of foci increased, the MI decreased accordingly.

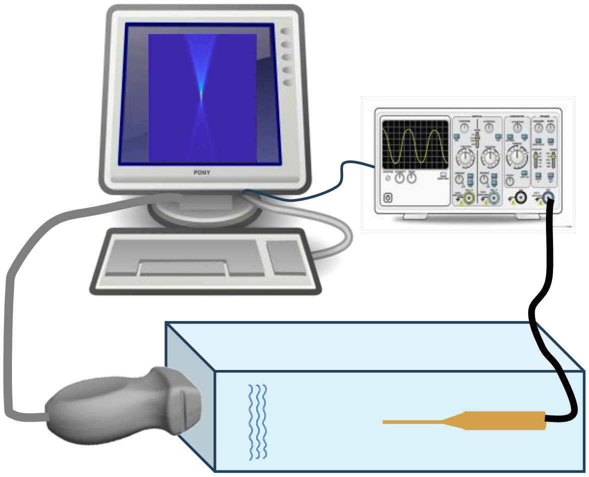

Figure 4. Schematic diagram of the experimental setup

5 Results

5.1 Validation of GASM and the STAR algorithm

To validate the quality of the propagation achieved using the GASM for pulses, a comparative analysis was conducted with the propagation performed using the k-Wave toolbox. The comparison was carried out across various patterns and at multiple depths. The transmitted delays for each pattern were computed using either the STAR or the GS algorithms. These algorithms were used to generate patterns with both well-separated foci and less-distinguishable foci to assess performance under different conditions.

As a representative example, a 3-foci pattern was evaluated. The delays were computed, and the propagation was performed using both the GASM and the k-Wave toolbox to generate the pattern at a depth of 40 mm. The analysis was conducted over depths ranging from 25 mm to 55 mm relative to the transducer position. Three distinct foci, approximately 6 mm apart, were produced by both approaches and were symmetrically distributed about the center of the x-axis (FIG. 5(a) and FIG. 5(b)). To quantify the differences between the two methods, the mean relative error was calculated at various depths by comparing cross-sections of the propagation. At 40 mm depth, as shown in FIG. 5(d), the cross-sections nearly overlap, with a mean relative error of 1.49%. Across all investigated depths for this pattern, an average relative error of approximately 2% was observed. FIG. 5(c) provides a visual representation of these differences between the XZ-planes generated by GASM and k-Wave. A total of 100 distinct patterns across 300 depth levels (n = 30,000) were analyzed, resulting in a mean relative error of 4 ± 1.5%.

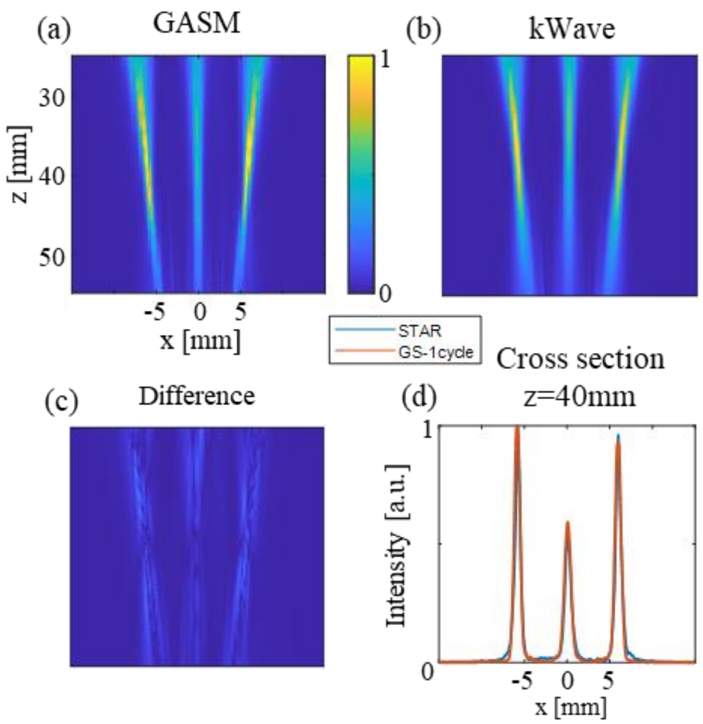

Figure 5. Comparison of pulse propagation using GASM and the k-Wave toolbox for a 3-foci pattern at a depth of 40 mm. The foci are spaced approximately 6 mm apart and symmetrically distributed along the x-axis. (a) Normalized intensity distribution in the XZ-plane obtained using GASM, where X represents the lateral direction and Z the axial direction. (b) Corresponding XZ-plane distribution using the k-Wave toolbox. (c) Visual representation of differences between the XZ-plane results from GASM and k-Wave. (d) Cross-section comparison at 40 mm depth.

After implementing the propagation methods and the GS algorithm, its output was validated. The simplest pattern to test was a single focus at a specific depth, as it allows for direct comparison with an analytical geometrical solution for the delays, given by the negative of the distance of each element divided by the speed of sound. The wavefronts obtained using the algorithm with an input pattern of one focus at the center of the lateral axis, at a depth of 40 mm and a frequency of 4.46 MHz, are shown in FIG. 6(a).

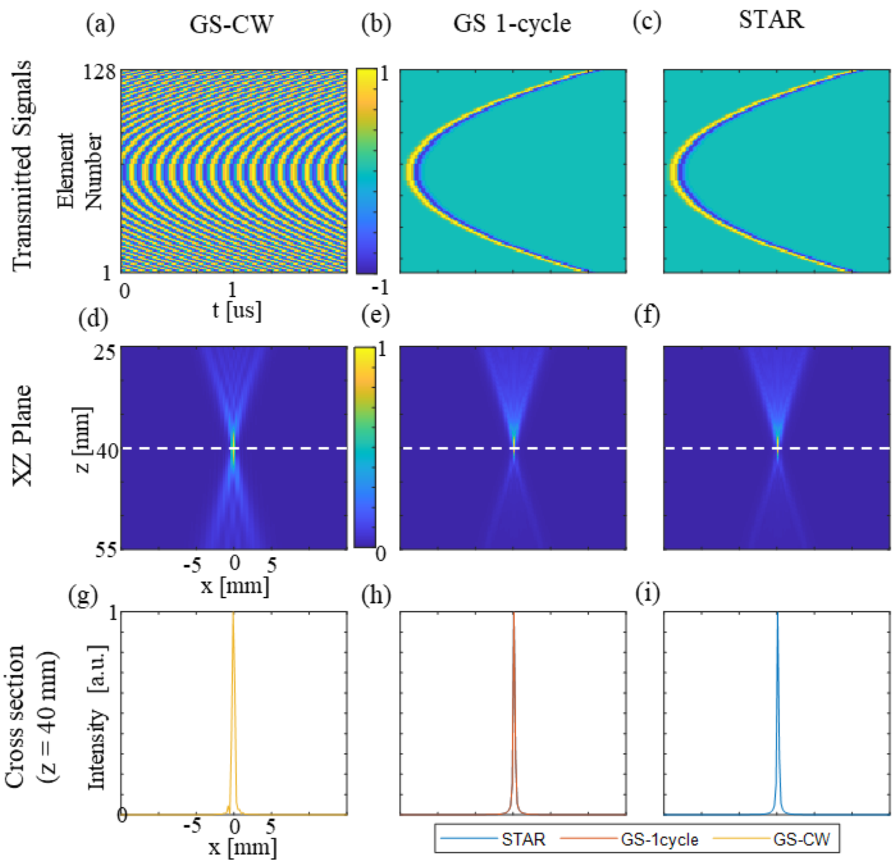

Figure 6. **Validation of the GS and STAR algorithms for a single-focus pattern at a depth of 40 mm (4.46 MHz).** (a) Wavefronts generated using the GS algorithm with an input pattern of a single focus at the center of the lateral axis. (b) Corresponding wavefronts for single-cycle excitation. (c) Wavefronts from the STAR algorithm. (d–f) XZ-plane intensity distributions from GS with CW excitation, GS with single-cycle excitation, and STAR, respectively. (g–i) Cross-section comparisons at 40 mm depth for the three cases

The output delays match those derived from the analytical geometrical solution, as confirmed by the XZ plane computed through propagation, which accurately reproduces the desired pattern (FIG. 6(d)) and its cross-section (FIG. 6(g)). As expected, applying these delays to a single-cycle excitation also generates the desired pattern, as shown in the second column of FIG. 6. Subsequently, the STAR algorithm was tested using the same pattern and produced identical results, as shown in the right column of the figure. This confirms that the STAR algorithm converges to both the GS algorithm and the analytical solution for the simple yet fundamental pattern of a single focus at the target depth.

5.2 Comparison of the GS and STAR algorithms for a simple pattern

After validating the propagation methods, the implementation and convergence of the GS algorithm to the geometrical solution, and the convergence of the STAR algorithm to the GS algorithm in the simple case of a single focus, an example is presented comparing the output of the STAR algorithm to the conventional GS algorithm (FIG. 7). In this example, both algorithms were tasked with generating a 3-foci pattern at a depth of 40 mm, with a spacing of 19 pitches (~4.15 mm) between each pair of foci, centered around the x-axis. To examine the differences between the methods and the impact of signal duration, signal propagation was computed using the GS output delays for both continuous-wave (CW) and single-cycle excitation, as well as using the STAR output delays for single-cycle excitation.

The transmitted signals generated from the phases output by the GS algorithm are illustrated by the signal amplitudes over time for each element (FIG. 7(a)). In this case, with CW excitation, the signals are periodic and consist of multiple cycles. The corresponding acoustic field propagation for this signal is shown with the target depth marked by a white line (FIG. 7(d)). The algorithm achieves accurate results in terms of the location and amplitude of the desired foci, producing three distinct foci precisely at the target depth.

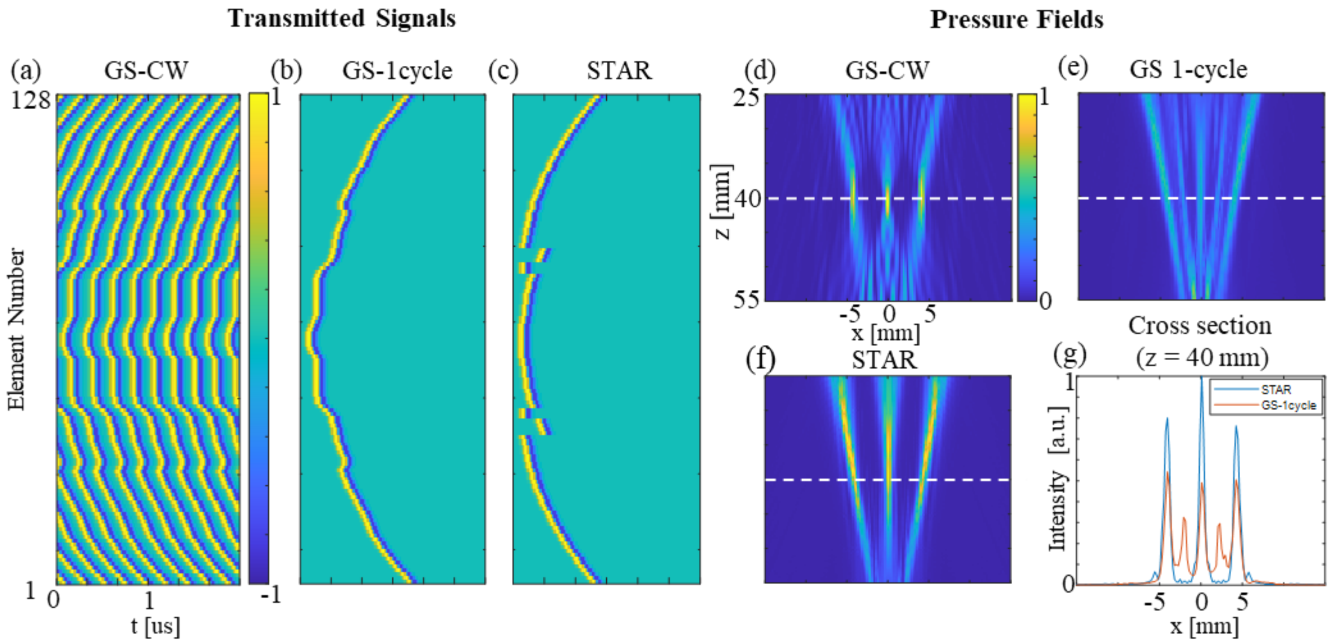

Figure 7. Comparison of the GS and STAR algorithms for generating a 3-foci pattern at 40 mm depth. (a) Transmitted signals for GS output delays with continuous-wave (CW) excitation, with color indicating signal amplitude. (b) Transmitted signals for GS output delays with single-cycle excitation. (c) Transmitted signals for STAR output delays with single-cycle excitation. (d) Propagated acoustic field for GS with CW excitation, with white lines marking the target depth. (e) Propagated acoustic field for GS with single-cycle excitation. (f) Propagated acoustic field for STAR with single-cycle excitation. (g) Cross-section comparisons at 40 mm.

However, when using a single-cycle excitation (FIG. 7(b)), the propagated acoustic field (FIG. 7(e)) exhibits less well-defined foci. While three foci are present at the desired locations, two undesired sidelobes appear between them. In contrast, the transmitted signals and propagated acoustic field based on the STAR algorithm delays are shown in FIGS. 7(c) and 7(f), respectively. Both FIGS. 7(e) and 7(f) are normalized to the same scale to enable a fair comparison, as the emitted energy is identical in both cases due to the single-cycle excitation.

The propagated field from the STAR output was similar to the desired pattern, with three clearly distinguished foci located precisely at the target depth and with heights closely matching the desired values. The cross-sections at the target depth highlight the superior energy concentration at 40 mm achieved with the STAR algorithm compared to the GS algorithm (FIG. 7(g)). The STAR output more closely resembles the desired pattern, effectively demonstrating its advantages in single-cycle excitation scenarios.

5.3 Investigation of key parameters

While implementing the STAR algorithm, the evolution of key parameters over multiple iterations was investigated. Two primary metrics were analyzed to track their changes across iterations in different examples. An illustrative example is provided using a desired pattern of three foci (FIG. 8). The normalized cross-correlation between the desired and output patterns was examined as a function of the number of iterations (FIG. 8(b)).

The GS algorithm converges within a small number of iterations. This behavior is evident, along with a decrease in correlation when switching from CW to single-cycle excitation. However, the STAR algorithm consistently achieves higher correlation values for the same task starting from the second iteration (FIG. 8(b)). Across all cases, the correlation stabilizes after the initial iterations and does not vary significantly thereafter. In contrast, the Peaks Uniformity Coefficient exhibits substantial variability throughout the iterations. A higher number of iterations does not necessarily lead to better uniformity, even if the correlation improves (FIG. 8(e)). This trend is further demonstrated by comparing acoustic fields computed at two different iterations of the STAR algorithm (FIG. 8(a) vs. FIG, 8(c)). By comparing the cross-sections at the target depth, it becomes apparent that the STAR output after 5 iterations better matches the desired pattern in terms of uniform peak heights, despite the correlation being slightly higher after 20 iterations (FIGS. 8(d) and 8(f)). This behavior was consistently observed across different patterns, leading to the incorporation of the Peaks Uniformity Coefficient as an additional factor in the stopping criteria and in selecting the specific iteration for output generation.

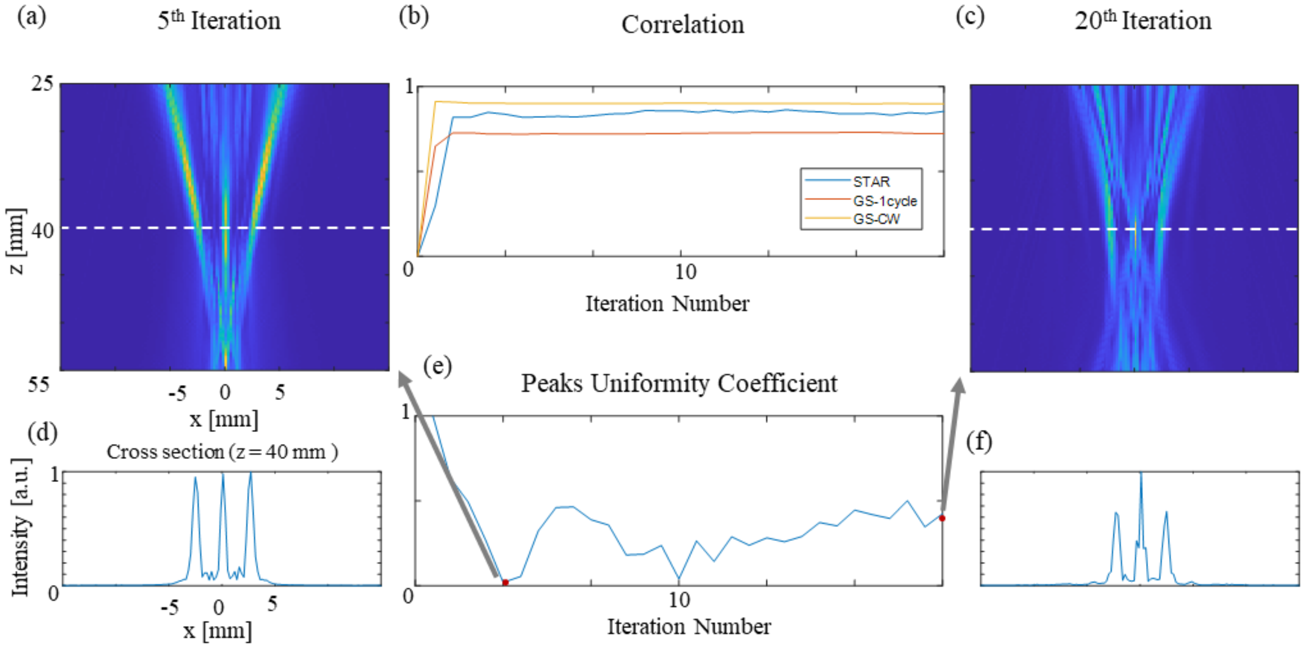

Figure 8. Evolution of key parameters during STAR algorithm iterations for a 3-foci pattern. (a) Output acoustic field after 5 iterations. (b) Normalized cross-correlation between the desired and output patterns as a function of iteration number: GS with CW excitation (yellow), GS with single-cycle excitation (orange), and STAR with single-cycle excitation (blue). (c) Output acoustic field after 20 iterations. (d) Cross-section at 40 mm depth for the STAR output after 5 iterations. (e) Peaks Uniformity Coefficient over iterations. (f) Cross-section at 40 mm depth for the STAR output after 20 iterations.

5.4 Performance Comparison of GS and STAR Across Patterns, Depths, and Frequencies

The STAR algorithm was tested across various patterns, including configurations with different numbers of foci, varying spacing between adjacent foci, and symmetric or asymmetric arrangements around the lateral axis. The main findings are illustrated through three representative examples (FIG. 9). Each row in FIG. 9 corresponds to a different desired pattern, while each column represents a specific algorithm or excitation type.

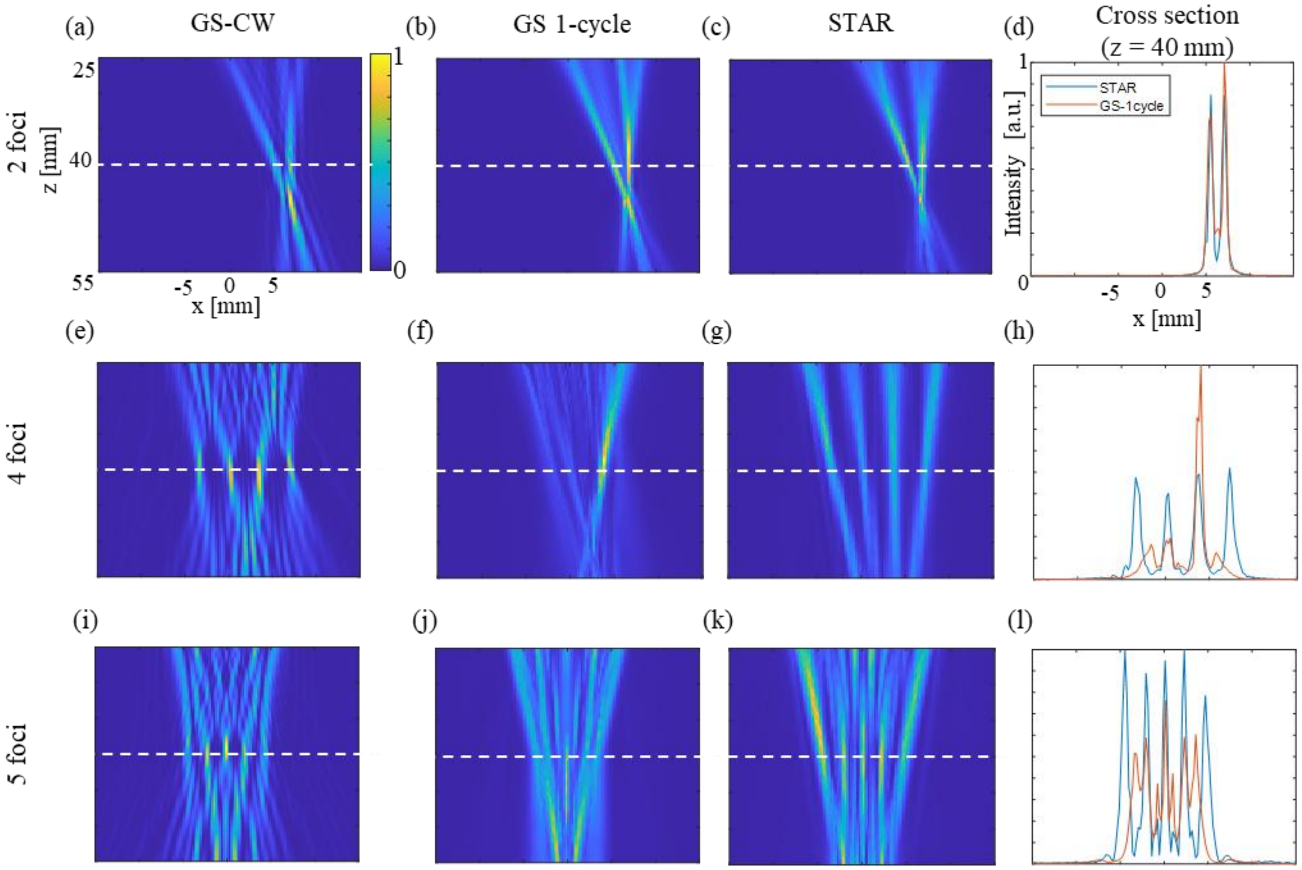

Figure 9. Comparison of GS and STAR algorithm performance across different multi-focus patterns: (a) XZ-plane intensity distribution for a two-foci pattern with a spacing of approximately 1.5 mm (7 pitches) and a 6 mm lateral offset, obtained using GS with CW excitation. (b) XZ-plane intensity distribution for the same pattern using GS with single-cycle excitation. (c) XZ-plane intensity distribution using STAR with single-cycle excitation. (d) Cross-section comparisons at the target depth of 40 mm for the two-foci pattern. (e) XZ-plane intensity distribution for a four-foci pattern with a spacing of approximately 3.5 mm (16 pitches) and a 3.5 mm lateral offset, obtained using GS with CW excitation. (f) XZ-plane intensity distribution for the same pattern using GS with single-cycle excitation. (g) XZ-plane intensity distribution using STAR with single-cycle excitation. (h) Cross-section comparisons at the target depth of 40 mm for the four-foci pattern. (i) XZ-plane intensity distribution for a five-foci pattern symmetrically arranged around the lateral axis, with a spacing of approximately 2.2 mm (10 pitches) between each pair, obtained using GS with CW excitation. (j) XZ-plane intensity distribution for the same pattern using GS with single-cycle excitation. (k) XZ-plane intensity distribution using STAR with single-cycle excitation. (l) Cross-section comparisons at the target depth of 40 mm for the five-foci pattern.

The first pattern involved two foci spaced approximately 1.5 mm apart, with an offset of about 6 mm from the center of the lateral axis. Both GS and STAR algorithms successfully generated this pattern, concentrating similar amounts of energy at the target depth (FIGS. 9(b), 9(c)). However, the STAR algorithm achieved a more balanced energy distribution between the two foci and produced a shallower null region between them—half as deep compared to the GS output (FIG. 9(d)). While the improvements provided by STAR for two-foci patterns with single-cycle excitation were relatively modest, since GS already performed well, STAR still achieved slightly better results. For instance, the correlation with the desired pattern was 0.869 for STAR compared to 0.861 for GS, reflecting an improvement of approximately 1%.

As the number of foci increased, the performance differences became more noticeable. The second pattern consisted of four foci spaced roughly 3.5 mm apart, with an offset of approximately 3.5 mm from the center of the lateral axis. In contrast, STAR successfully generated four nearly equal foci at the target depth (FIG. 9(g)). While the total energy at the target depth was only slightly higher in the STAR case, the energy distribution was more uniform between the foci (FIG. 9(h)). This improvement is also reflected in the correlation values, with STAR achieving 0.80 compared to 0.64 for GS.

Additionally, as the number of foci increased, the accuracy of the GS output decreased relative to STAR. Specifically, positional errors became more pronounced—for example, in this case, the leftmost and rightmost foci were misplaced in the GS single-cycle output. The third pattern involved five foci symmetrically arranged around the lateral axis, with a spacing of approximately 2.2 mm (10 pitches) between each pair. Similar to previous cases, GS performed well for CW excitation (FIG. 9(i)) but failed to generate five distinct foci under single-cycle excitation (FIG. 9(j)). The foci were not well-defined, and the null regions between them were too high. However, STAR successfully produced the pattern, with accurate focal positions and minimal variation in peak heights (FIG. 9(k)). Notably, GS struggled with foci located further from the center of the lateral axis. While the two foci adjacent to the central one were positioned correctly, the outermost two were shifted closer to the center (FIG. 9(l)). Across all three patterns, and in approximately 95% of the tested patterns, the correlation between STAR results and the desired patterns was consistently higher than that of GS results. For two or more foci, GS achieved the highest correlation under CW excitation, as expected. However, STAR consistently outperformed GS in single-cycle excitation, particularly as the number of foci increased, ensuring better energy distribution, positional accuracy, and peak uniformity.

After evaluating the success of the STAR algorithm with various patterns at a depth of 40 mm and a frequency of 4.5 MHz, the scope of the research was expanded to include different target depths and frequencies. In the STAR algorithm, both parameters are defined as input values, similar to the GS algorithm. For this comparison, several patterns were tested. The presented example (FIG. 10) focuses on a 3-foci pattern symmetrically distributed around the center of the lateral axis, with a spacing of 12 pitches (~2.6 mm) between each pair of foci. Both algorithms were tasked with generating this pattern at different target depths (30 mm, 40 mm, and 50 mm are displayed in FIG. 10).

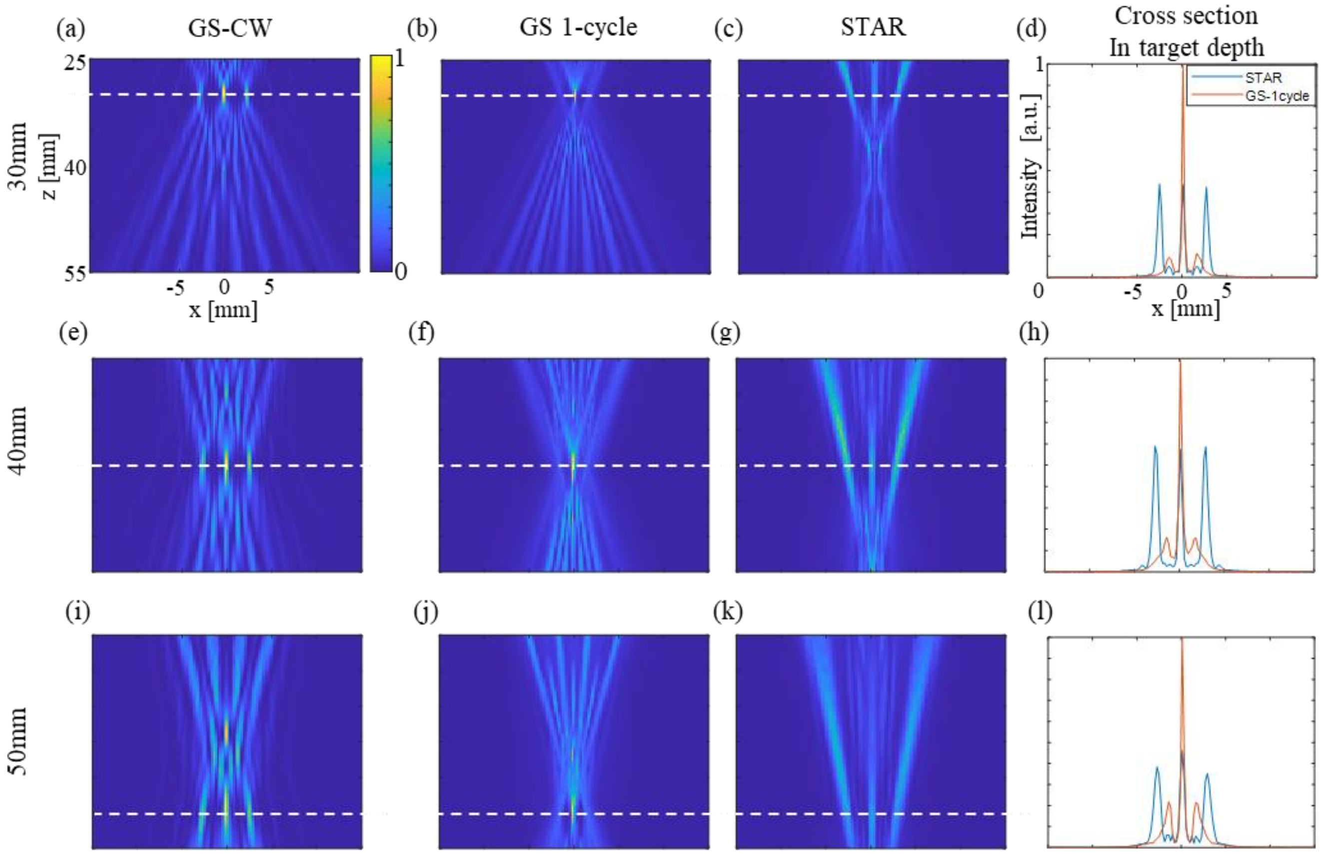

Figure 10. Comparison of GS and STAR algorithm performance for a 3-foci pattern with 12-pitch spacing (~2.6 mm) between each pair of foci at different target depths. (a) XZ-plane intensity distribution at 30 mm depth using GS with CW excitation. (b) XZ-plane intensity distribution at 30 mm depth using GS with single-cycle excitation. (c) XZ-plane intensity distribution at 30 mm depth using STAR with single-cycle excitation. (d) Cross-section comparisons at 30 mm depth. (e) XZ-plane intensity distribution at 40 mm depth using GS with CW excitation. (f) XZ-plane intensity distribution at 40 mm depth using GS with single-cycle excitation. (g) XZ-plane intensity distribution at 40 mm depth using STAR with single-cycle excitation. (h) Cross-section comparisons at 40 mm depth. (i) XZ-plane intensity distribution at 50 mm depth using GS with CW excitation. (j) XZ-plane intensity distribution at 50 mm depth using GS with single-cycle excitation. (k) XZ-plane intensity distribution at 50 mm depth using STAR with single-cycle excitation. (l) Cross-section comparisons at 50 mm depth.

The GS algorithm performs well under CW excitation at all target depths, achieving a correlation of over 0.9 in all cases (FIGS. 10(a), 10(e), 10(i)). The resulting patterns exhibit foci at the exact desired locations, with three distinct foci of slightly varying heights due to the apodization constraint, which was set to 1 for all elements. Allowing flexibility in apodization would equalize the foci heights and improve correlation, bringing it closer to 1, but would result in energy loss. However, with single-cycle excitation, the GS algorithm shows significant degradation in performance (FIGS. 10(b), 10(f), 10(j)). The typical pattern consists of a high central focus on the lateral axis with two smaller, smeared foci. These smaller foci are not at the desired locations and are 5 to 10 times lower in height than the central focus (FIGS. 10(d), 10(h), and 10(l)). This degradation is also evident in the correlation values, which are 0.55, 0.69, and 0.62 for target depths of 30 mm, 40 mm, and 50 mm, respectively.

In contrast, the STAR algorithm performs consistently well across all examined depths. The 3-foci pattern is accurately generated, with the foci located at the intended positions and of equal heights (FIGS. 10(c), 10(g), 10(k)). The correlation values are also much higher (0.82, 0.82, and 0.77). Although the two off-center foci exhibit slightly greater widths than the central focus, the STAR output distributes energy more evenly among the three foci compared to the GS output. While the GS single-cycle propagation results exhibit a higher central focus, the STAR output is superior in achieving equal focus heights and distributing energy more evenly among the three foci, which is a critical aspect of the desired pattern.

In addition to testing different depths, the algorithms were also evaluated at various frequencies around the transducer's center frequency. FIG. 11 presents results for the same 3-foci pattern at a depth of 40 mm with frequencies of 3.5 MHz, 4.5 MHz, and 5.5 MHz. Across all tested frequencies, the STAR algorithm demonstrated superior performance compared to the GS algorithm, particularly in achieving uniform foci and consistent focus heights.

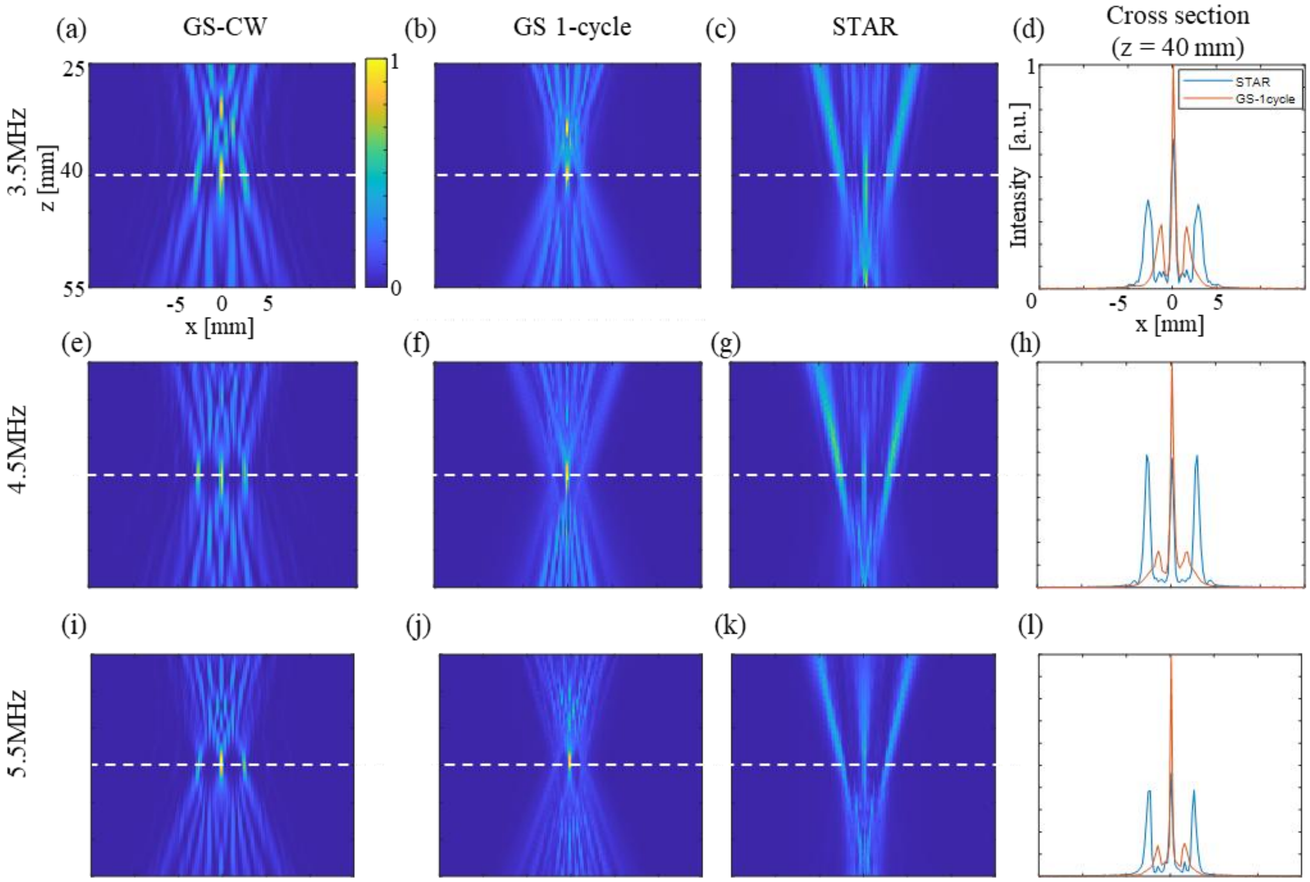

Figure 11. Comparison of GS and STAR algorithm performance for a 3-foci pattern with 12-pitch spacing (~2.6 mm) between each pair of foci at 40 mm depth across different frequencies. (a) XZ-plane intensity distribution at 3.5 MHz using GS with CW excitation. (b) XZ-plane intensity distribution at 3.5 MHz using GS with single-cycle excitation. (c) XZ-plane intensity distribution at 3.5 MHz using STAR with single-cycle excitation. (d) Cross-section comparisons at 3.5 MHz. (e) XZ-plane intensity distribution at 4.5 MHz using GS with CW excitation. (f) XZ-plane intensity distribution at 4.5 MHz using GS with single-cycle excitation. (g) XZ-plane intensity distribution at 4.5 MHz using STAR with single-cycle excitation. (h) Cross-section comparisons at 4.5 MHz. (i) XZ-plane intensity distribution at 5.5 MHz using GS with CW excitation. (j) XZ-plane intensity distribution at 5.5 MHz using GS with single-cycle excitation. (k) XZ-plane intensity distribution at 5.5 MHz using STAR with single-cycle excitation. (l) Cross-section comparisons at 5.5 MHz

The STAR algorithm achieved significantly higher correlation values (0.72, 0.82, and 0.76) compared to GS (0.54, 0.69, and 0.54) at frequencies of 3.5 MHz, 4.5 MHz, and 5.5 MHz, respectively. The GS algorithm consistently produced a higher central focus, accompanied by two smaller, less distinct foci that were mispositioned and asymmetrically smeared. The best results for uniformity and focus height were achieved at 4.5 MHz, likely due to it being the transducer’s center frequency. In general, as the frequency decreases, the average width of the foci increases, which is consistent with the expected degradation in lateral resolution at lower frequencies. This trend was observed in both GS and STAR algorithm outputs, as expected.

5.5 Resolution Analysis: Minimum Achievable Foci Spacing with GS and STAR

To evaluate the resolution improvement achieved by the STAR algorithm, it was of interest to determine whether STAR could generate patterns with closer foci compared to the GS algorithm. The process was as follows: the algorithms were tasked with generating two foci at progressively smaller spacings, aiming to reduce the spacing until the foci could no longer be distinguished (FIG. 12). The results indicate that both algorithms fail to produce two distinguishable foci at a spacing of 2 pitches and struggle at 3 pitches, although the STAR algorithm visually performs better in this case. However, while the GS algorithm fails to generate two distinct foci at a spacing of 4 pitches, the STAR algorithm successfully resolves them. Foci are considered distinguishable if the intensity between them drops to less than half of the maximum intensity of the smaller focus. Under the parameters of this study, the minimum achievable spacing was improved from 1.09 mm with the GS algorithm to 0.872 mm with the

STAR algorithm for single-cycle excitation. Additionally, for larger distances, both algorithms successfully generated distinct foci.

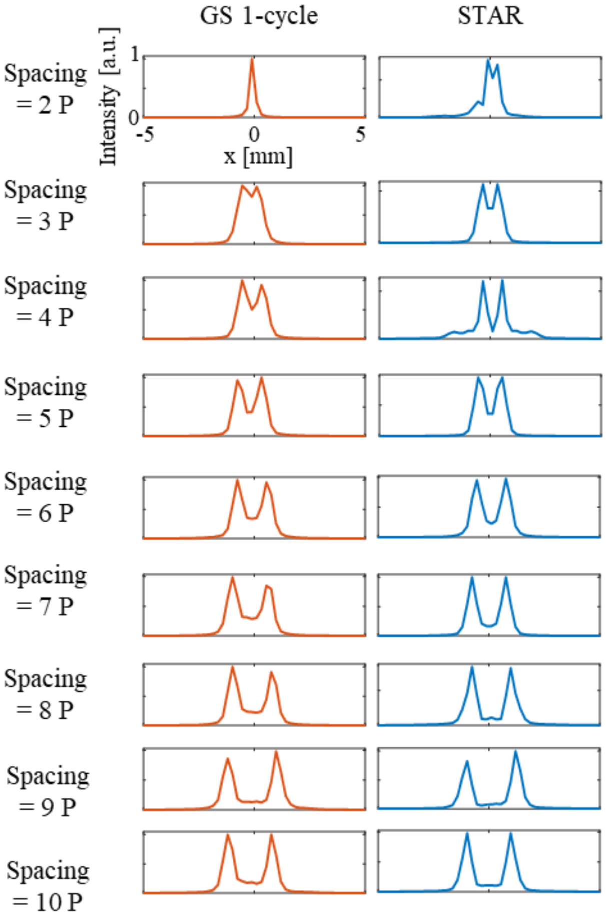

Figure 12. Resolution test - Comparison of GS and STAR algorithm performance in generating closely spaced. Cross-sections at the target depth for progressively increasing foci spacings. The left column shows the cross-section obtained from GS with single-cycle ex

5.6 Effect of number of foci on pressure intensity and uniformity

When increasing the number of foci, a decrease in the average height of the foci is expected due to the redistribution of finite acoustic energy among a larger number of focal points. This behavior is confirmed in the STAR algorithm outputs (FIG. 13(a)). The algorithm was tested across hundreds of patterns with varying numbers of foci and different spacings between adjacent foci. For each configuration, the pressure intensity at each focus was measured, and the mean pressure intensity was calculated. The results demonstrate a clear decrease in mean pressure as the number of foci increases.

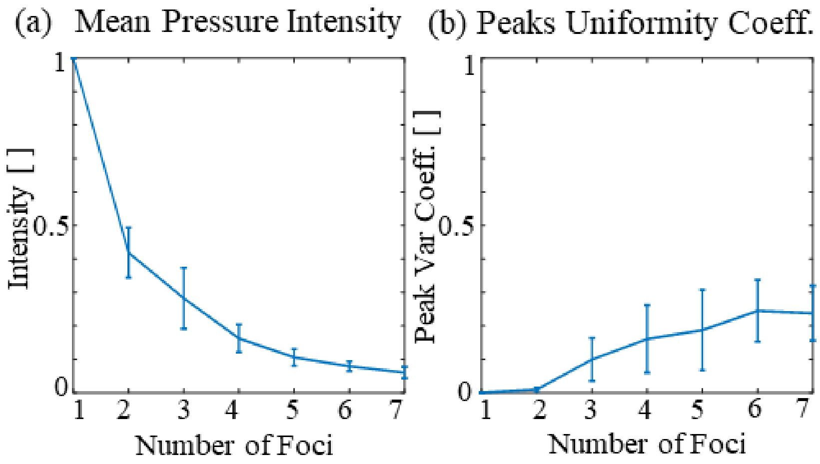

Figure 13. Effect of increasing the number of foci. (a) Mean pressure intensity at each focus as a function of the number of foci, measured across various patterns with varying numbers of foci and different spacings between each pair of foci. (b) Mean Peaks Uniformity Coefficient as a function of the number of foci, measured across the same patterns.

Additionally, the uniformity of focal peaks was analyzed using the Peaks Uniformity Coefficient, which was calculated for the same dataset (FIG. 13(b)). This parameter correlates with the difficulty of generating the desired pattern, assuming all foci are of equal height. The results show that as the number of foci increases, the Peaks Uniformity Coefficient also increases, although it remains relatively low. This finding aligns with the observation that patterns with one or two foci are generated with high accuracy and uniformity, while patterns with a larger number of foci occasionally display unequal energy distribution. This challenge becomes more evident as the number of foci increases, as highlighted in FIG. 13(b) and supported by FIG.9.

5.7 Experimental validation of the STAR algorithm

To validate the proposed algorithm, experimental measurements were conducted using the setup described in the Methods section (FIG. 14). Four patterns were tested experimentally. Each column in the figure corresponds to a different pattern, and each row represents a specific algorithm or signal duration. It should be noted that both XZ planes from the GS single-cycle and STAR outputs for the same desired pattern were normalized to the same scale to ensure a fair comparison, as the emitted energy was identical in both cases due to the single-cycle excitation.

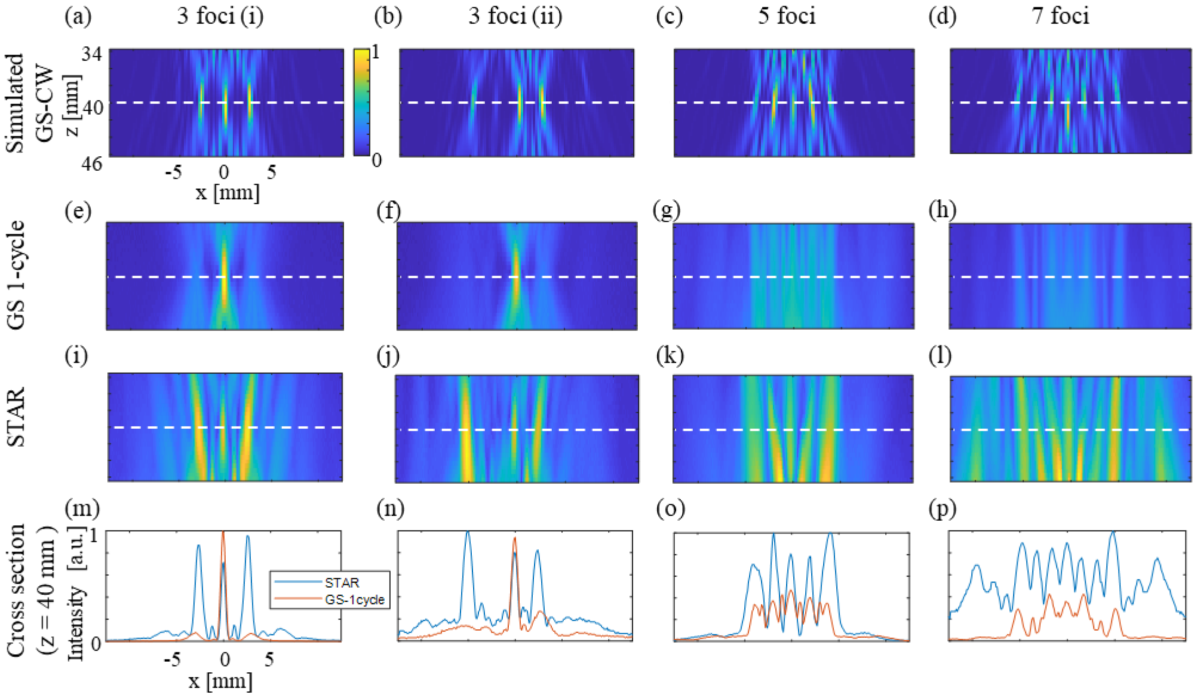

Figure 14. Experimental validation of GS and STAR algorithm performance for multi-focus patterns. Each column represents a different tested pattern, and each row corresponds to a different algorithm or excitation. The first pattern consists of three symmetrically arranged foci with 12-pitch spacing. The second pattern features three asymmetrically spaced foci (11 and 23 pitches). The third pattern consists of five foci with 9-pitch spacing. The final pattern contains seven foci with 8-pitch spacing. (a–d) XZ-plane intensity distributions from simulations of continuous-wave (CW) propagation using GS-derived delays. (e–h) Measured acoustic fields from hydrophone recordings for XZ planes generated using GS-derived delays with single-cycle excitation. (i–l) Measured acoustic fields from hydrophone recordings for XZ planes generated using STAR-derived delays with single-cycle excitation. (m–p) Cross-section comparisons at the target depth of 40 mm for GS and STAR outputs.

The first pattern tested consisted of three foci symmetrically arranged around the central x-axis with a spacing of 12 pitches. The acoustic field measured for the GS single-cycle excitation (FIG. 14(e)) closely matches the simulated result from FIG. 10(f). Similarly, the acoustic field measured for the STAR output (FIG. 14(i)) correlates well with the simulation shown in FIG. 10(g). The measured cross-sections (FIG. 14(m)) also validate the simulation results from FIG. 10(h). Interestingly, in terms of energy distribution, the STAR algorithm demonstrated even better performance than predicted by the simulation, achieving higher relative focal intensities compared to the GS single-cycle cross-section. The GS output exhibited the typical pattern of one dominant focus with two weaker, smeared side foci. Conversely, the STAR output produced three foci with relatively close intensities, though not perfectly equal. The second pattern tested included three foci with unequal spacings (11 pitches and 23 pitches) arranged asymmetrically around the x-axis. The GS algorithm struggled to generate this pattern with single-cycle excitation, whereas the STAR algorithm demonstrated significantly superior performance (FIG. 14(n)). The difference in performance was even more evident in the third pattern, which consisted of five foci with equal spacing (9 pitches). The acoustic field generated from the GS output for this pattern did not adequately reproduce the desired configuration, making it challenging to identify the original pattern (FIG. 14(g)). In contrast, the STAR algorithm successfully generated five foci with nearly equal intensities at the specified positions. The higher relative intensity of the STAR-generated foci, compared to GS, further highlights its ability to concentrate energy more effectively at the target depth (FIG. 14(o)). Additionally, it was consistently observed that foci located further from the center of the lateral axis tended to be broader. This behavior was apparent across all patterns and was particularly evident in FIG. 14(o). The final pattern consisted of seven foci with a spacing of 8 pitches between each pair. Both algorithms exhibited limitations in generating this pattern effectively in the experiments (FIG. 14(p)). For the GS single-cycle output, the foci were weak and indistinct. The STAR algorithm produced high side lobes in addition to the desired pattern. Although the foci generated by the STAR algorithm were not completely distinct, they were more distinguishable compared to the GS output.

6 Discussion

This study presents the STAR algorithm as a generalized beam-shaping method for ultra-short pulses across wave-based technologies, with its capabilities demonstrated in the field of medical ultrasound. Specifically, the STAR algorithm enables the efficient and accurate generation of multi-foci patterns for ultra-short pulses, including signals as short as a single cycle. By leveraging time-domain optimization, the STAR algorithm addresses the limitations of traditional phase-domain methods, enabling precise control over acoustic field generation. A critical component of the STAR implementation is the integration of the GASM, which facilitates efficient and rapid propagation of ultrasound pulses.

The results confirm the accuracy of the GASM in computing the propagation of acoustic fields, as validated by its strong agreement with the k-Wave toolbox across various patterns and depths. Moreover, the GASM exhibits high computational efficiency for computing the propagation to specific depths of interest, achieving computation times that are several orders of magnitude faster. This efficiency arises from its reliance on FFT-based computations and its focus on specific planes rather than entire volumetric grids. Additionally, the GASM's support for back-propagation enhances its suitability for iterative algorithms like the STAR, which leverages back-propagation to transition between different parallel planes.

The STAR algorithm consistently outperforms the conventional GS algorithm in generating multi-foci patterns with single-cycle excitation. For simple patterns, such as a single focus, the STAR algorithm converges to the GS solution, aligning with the analytical geometrical solution.

Since this solution is considered ideal for this pattern, it serves as a reliable validation step for both the GS implementation and the STAR approach. However, the advantages of the STAR algorithm become particularly pronounced as the complexity of the desired patterns increases.

For instance, in a 3-foci pattern at a depth of 40 mm, the STAR algorithm achieved superior energy concentration and spatial accuracy compared to the GS algorithm. The normalized cross-sections at the target depth revealed that the STAR output more closely resembled the desired pattern, with minimal sidelobes and uniform focus heights. This trend persisted across various configurations, including patterns with increasing numbers of foci, varying lateral spacings, and asymmetric arrangements. The improvements in energy distribution and positional accuracy with the STAR algorithm were consistently demonstrated, even in challenging scenarios such as five-foci patterns.

The robustness of the STAR algorithm was demonstrated through its superior performance over the GS algorithm across varying target depths (30 mm, 40 mm, 50 mm) and excitation frequencies (3.5 MHz, 4.5 MHz, 5.5 MHz). The STAR consistently achieved higher correlation values, more uniform focus heights, and greater positional accuracy, even at larger or smaller depths and off-center frequencies, where the GS algorithm struggled with smeared and misplaced foci. These findings highlight the STAR algorithm's versatility and potential for diverse applications. The best results for uniformity and focus height were observed at 4.5 MHz, likely due to it being the transducer’s center frequency. In general, as the frequency decreases, the average width of the foci increases, which aligns with the expected degradation in lateral resolution at lower frequencies. This trend was consistently observed in both GS and STAR algorithm outputs.

A critical evaluation was performed to determine the ability of the STAR algorithm to generate closely spaced foci. As shown in FIG. 12, using single-cycle excitation, the minimum distinguishable spacing improved from 1.09 mm with the GS algorithm to 0.872 mm with the STAR algorithm. This capability underscores the STAR algorithm's potential for enhancing resolution in advanced imaging applications.

The performance of the STAR algorithm in generating patterns with varying numbers of foci was systematically analyzed, as illustrated in FIG. 13. Increasing the number of foci led to a predictable decrease in mean pressure intensity (FIG. 13(a)). While this reduction was slightly steeper than anticipated, the values remained within an acceptable range. Interestingly, this behavior aligns with the observation that as foci are placed farther from the lateral axis center, their widths tend to increase, as visualized in FIG. 14(o). As the number of foci increases, some are positioned farther from the center of the lateral axis. If their average distance increases, their average width also becomes larger, leading to a steeper decrease in the mean height of the foci relative to a linear decrease. This spatial broadening contributes to the steeper-than-expected decrease in mean pressure intensity, as noted in FIG. 13(a).

The Peaks uniformity coefficient revealed that patterns with one or two foci were generated with high accuracy and uniformity, while patterns with a larger number of foci displayed occasional unequal energy distribution. This trend highlights the challenges associated with generating complex patterns but also affirms the robustness of the STAR algorithm in maintaining reasonable uniformity.

One of the key contributions of this work is the optimization of beam profiles in the time domain rather than the phase domain. The iterative process of the GS algorithm is performed on the wrapped phase values, with unwrapping applied only after convergence to prepare the phase distribution for implementation. Optimizing in the time domain allows for precise handling of abrupt changes or delays that phase optimization and unwrapping cannot effectively address. By directly dealing with signal propagation over time, the STAR algorithm exploits time-domain characteristics, enabling better performance and accuracy in scenarios where phase-based methods encounter limitations.

Furthermore, the inclusion of single-cycle excitations as an adjustable parameter in the algorithm enhances its adaptability. This flexibility ensures that signal duration is inherently considered during the iterative process, improving the algorithm’s applicability across a range of scenarios, including ultrasound imaging. For different applications, the algorithm can also account for the desired pulse duration, allowing optimization to be tailored to specific requirements, ensuring its suitability for a wide variety of use cases.

Experimental validation using hydrophone measurements further confirmed the accuracy and practicality of the proposed methods. The measured acoustic fields closely matched simulation results, with the STAR algorithm consistently outperforming the GS algorithm for single-cycle excitation. For example, in patterns with three foci, the STAR produced more distinct and uniform foci compared to the GS, which exhibited smeared and uneven focus intensities. The

STAR algorithm also excelled in generating more complex patterns, such as five foci with equal spacing, where the GS struggled to replicate the desired configuration.

The STAR algorithm’s superior energy distribution was particularly evident in experimental setups, achieving higher relative focal intensities and more consistent pattern reproduction. While challenges remained for extremely complex patterns, such as seven foci with close spacing, the STAR algorithm demonstrated a clear advantage in terms of focus distinguishability and energy concentration.

The iterative behavior of the STAR algorithm reveals that while the normalized cross-correlation stabilizes after a few iterations, the Peaks Uniformity Coefficient can vary significantly. This indicates that higher correlation values do not always correspond to better focus uniformity. Incorporating additional metrics, such as the Peaks Uniformity Coefficient, into the stopping criteria can increase performance for specific purposes. However, considering this metric introduces a limitation when generating holograms with varying focus heights. This was provided as an example, and different metrics can be adopted depending on the scenario.

Future research should aim to extend the applications of the STAR algorithm. For example, leveraging STAR-generated patterns to enhance the Acoustical Structured Illumination (ASI) method could improve super-resolution imaging capabilities. Additionally, integrating the STAR with full imaging schemes, encompassing both transmission and reception, could yield further insights and advancements in ultrasound imaging.

Beyond ultrasound, the adaptability of the time-domain optimization approach opens opportunities for applications in optics, radar, and photoacoustics, where precise wavefront shaping of ultra-short pulses is crucial.

Moreover, the integration of the GASM into other phase-domain algorithms could address complex challenges. Future investigations could explore the use of polychromatic waves and diverse pulse shapes to further optimize pattern generation, taking advantage of the STAR algorithm's capability to handle any time-domain signal.

In conclusion, the STAR algorithm, integrated with the GASM, provides a versatile and efficient framework with the potential to significantly enhance ultrasound imaging and other wave-based applications.

7 Conclusion

This study introduced the STAR algorithm as a generalized beam-shaping method for ultra-short pulses, demonstrated in the field of medical ultrasound. By integrating STAR with the GASM, the proposed approach achieves precise multi-foci generation while maintaining high computational efficiency, particularly for single-cycle excitations. This framework addresses key limitations of phase-based methods, offering improved spatial accuracy, energy distribution, and adaptability. The findings have significant implications for biomedical ultrasound, particularly in applications requiring precise control over acoustic fields, such as high-resolution imaging and therapy. The STAR algorithm consistently outperforms the GS algorithm, especially in scenarios involving closely spaced foci or complex beam patterns, positioning it as a promising solution for real-time, high-resolution ultrasound systems. Beyond ultrasound, this framework has broader relevance for wave-based technologies, including optics and acoustics, where accurate beam shaping of pulsed waves is critical. In summary, the STAR approach provides an efficient, adaptable, and computationally powerful solution for many wave-based applications.

8 References

[1] Ilovitsh, T., Ilovitsh, A., Foiret, J., Fite, B. Z., & Ferrara, K. W., Acoustical structured illumination for super-resolution ultrasound imaging. Communications biology, 1(1), 3. (2018).

[2] Grier, D. G. A revolution in optical manipulation. Nature (2003).

[3] David G. Grier and Yael Roichman, Holographic optical trapping, Appl. Opt. 45, 880-887 (2006).

[4] Horstmeyer, R., Ruan, H. & Yang, C., Guidestar-assisted wavefront-shaping methods for focusing light into biological tissue. Nature Photon 9, 563–571 https://doi.org/10.1038/nphoton.2015.140 (2015).

[5] Melde, K., Mark, A. G., Qiu, T., & Fischer, P., Holograms for acoustics. Nature, 537(7621), 518-522. (2016).

[6] Gerchberg, R. W., Saxton, W. O. A practical algorithm for the determination of phase from image and diffraction plane pictures. Optik, 35, pp 237-246. (1972).

[7] Yang Wu, Jun Wang, Chun Chen, Chan-Juan Liu, Feng-Ming Jin, and Ni Chen , Adaptive weighted Gerchberg-Saxton algorithm for generation of phase-only hologram with artifacts suppression (2021).

[8] Junqiao Pan, Chuan Shen, Ze Shen, Xiaodie Wang, Cheng Zhang, Sui Wei, Optimized adaptive weighted Gerchberg–Saxton algorithm for generation of phase-only hologram, Opt. Eng. 63(12) 123104 , (2024).

[9] Tieyu Zhao and Yingying Chi, Modified Gerchberg–Saxton (G-S) Algorithm and Its Application, Information Science Teaching and Research Section, Northeastern University at Qinhuangdao (2020).

[10] Haotong Ma, Zejin Liu, Xiaojun Xu, Sanhong Wang, and Changhai Liu, Near-diffraction-limited flattop laser beam adaptively generated by stochastic parallel gradient descent algorithm, Opt. Lett. 35, 2973-2975 (2010).

[11] Wu, Daixuan, et al., A thorough study on genetic algorithms in feedback-based wavefront shaping, Journal of Innovative Optical Health Sciences 12.04: 1942004. (2019).

[12] Fushimi, T., Yamamoto, K., & Ochiai, Y., Acoustic hologram optimisation using automatic differentiation. Scientific reports, 11(1), 12678. (2021).

[13] Wu, Y., Rivenson, Y., Zhang, Y., Wei, Z., Günaydin, H., Lin, X., & Ozcan, A. Extended depth-of-field in holographic imaging using deep-learning-based autofocusing and phase recovery. Optica, 5(6), 704-710. (2018).

[14] Rivenson, Y., et al., Phase recovery and holographic image reconstruction using deep learning in neural networks, Light: Science & Applications (2018).

[15] Chen, C. Y., Cheng, C. W., Chou, T. A., & Chuang, C. H., Real-time hologram generation using a non-iterative modified Gerchberg-Saxton algorithm. Optics Communications, 550, 130024. (2024).

[16] Moon Hwan Lee , Hah Min Lew , Sangyeon Youn , Tae Kim and Jae Youn Hwang, Deep Learning-Based Framework for Fast and Accurate Acoustic Hologram Generation ,IEEE Transactions on Ultrasonics Ferroelectrics and Frequency Control PP(99):1-1 (2022).

[17] Jiachen Wu, Kexuan Liu, Xiaomeng Sui, and Liangcai Cao, High-speed computer-generated holography using an autoencoder-based deep neural network, Opt. Lett. 46, 2908-2911 (2021).

[18] Lu, Q., Zhong, C., Su, H., & Liu, S., Physics-based generative adversarial network for real-time acoustic holography. Ultrasonics, 107583. (2025).

[19] Borzov, A. B., Likhoedenko, K. P., Seregin, G. M., & Suchkov, V. B., Applications of short-range radars on the base of ultrashort pulse single chip. In 2017 3rd IEEE International Conference on Control Science and Systems Engineering (ICCSSE) (pp. 461-464). (2017).

[20] Larson, A. M., Multiphoton microscopy (2011).

[21] Vicidomini, G., Bianchini, P., & Diaspro, A., STED super-resolved microscopy. Nature methods, 15(3), 173-182. (2018).

[22] Jauniaux, E., Johns, J., & Burton, G. J., The role of ultrasound imaging in diagnosing and investigating early pregnancy failure. Ultrasound in Obstetrics and Gynecology: The Official Journal of the International Society of Ultrasound in Obstetrics and Gynecology, 25(6), 613-624. (2005).

[23] Joyner Jr, C. R., & Reid, J. M., Applications of ultrasound in cardiology and cardiovascular physiology. Progress in cardiovascular diseases, 5(5), 482-497. (1963).

[24] Woodfield, C. A., The usefulness of ultrasound imaging in gynecologic oncology. PET clinics, 13(2), 143-163. (2018).

[25] Tempany, C. M., McDannold, N. J., Hynynen, K., & Jolesz, F. A., Focused ultrasound surgery in oncology: overview and principles. Radiology, 259(1), 39-56. (2011).

[26] Delaney, L. J., Isguven, S., Eisenbrey, J. R., Hickok, N. J., & Forsberg, F., Making waves: how ultrasound-targeted drug delivery is changing pharmaceutical approaches. Materials advances, 3(7), 3023-3040. (2022).

[27] Ng, A., & Swanevelder, J., Resolution in ultrasound imaging. Continuing Education in Anaesthesia, Critical Care & Pain, 11(5), 186-192. (2011).

[28] Schein, D., Grutman, T., & Ilovitsh, T., Deep learning-based ultrasound beam shaping for spatiotemporal acoustic holograms generation. IEEE Transactions on Ultrasonics, Ferroelectrics, and Frequency Control, 70(6), 551-561. (2023).

[29] Goodman, J. W., Introduction to Fourier optics. Roberts and Company publishers. (2005).

[30] Leeman, S., & Healey, A. J., Field propagation via the angular spectrum method. Acoustical Imaging, 363-368. (1997).

[31] Du, Y., Jensen, H., & Jensen, J. A., Investigation of an angular spectrum approach for pulsed ultrasound fields. Ultrasonics, 53(6), 1185-1191 (2013).

[32] Bakhru RN, Schweickert WD. Intensive care ultrasound: I. Physics, equipment, and image quality. Ann Am Thorac Soc. 2013 Oct;10(5):540-8

[33] Kremkrau FW. Diagnostic Ultrasound. 6th edition, W. B. Saunders Company, New York, 200

[34] Harris RA, Follett DH, Halliwell M, Wells PN. Ultimate limits in ultrasonic imaging resolution. Ultrasound Med Biol. 1991;17(6):547-58. doi: 10.1016/0301-5629(91)90025-r. PMID: 1962357.

[35] Li J, Ma Y, Zhang T, Shung KK, Zhu B. Recent Advancements in Ultrasound Transducer: From Material Strategies to Biomedical Applications. BME Front. 2022.

[36] A. Fenster and D. B. Downey, "3-D ultrasound imaging: a review," in IEEE Engineering in Medicine and Biology Magazine, vol. 15, no. 6, pp. 41-51, Nov.-Dec. 1996

[37] J. A. Jensen, “Estimation of blood velocities using ultrasound: a signal processing approach,” Cambridge University Press, 1996

[38] ter Haar G. Therapeutic applications of ultrasound. Prog Biophys Mol Biol. 2007 Jan-Apr;93(1-3):111-29.

[39] Díaz-Alejo JF, González Gómez I, Earl J. Ultrasounds in cancer therapy: A summary of their use and unexplored potential. Oncol Rev. 2022 Feb 22;16(1):531

[40] Melde, K., Mark, A., Qiu, T. *et al.* Holograms for acoustics. *Nature* 537, 518–522 (2016).

[41] Glickstein, O. Shaul, and T. Ilovitsh , Rationally designed acoustic holograms for uniform nanodroplet-mediated tissue ablation. IEEE Transactions on Ultrasonics, Ferroelectrics, and Frequency Control (2024)

[42] H. Shinar and T. Ilovitsh Volumetric Passive Acoustic Mapping and Cavitation Detection of Nanobubbles under Low-Frequency Insonation. ACS Materials Au (2024)

תקציר

עיצוב אלומה לפולסים קצרים מאוד מהווה אתגר משמעותי בטכנולוגיות המבוססות על גלים, שבהן נדרשת שליטה מדויקת בחזיתות הגל על מנת להשיג פיזור אנרגיה מסוים או תבניות מרחביות רצויות. שיטות לעיצוב אלומה קונבנציונליות, כגון אלגוריתם Gerchberg–Saxton הנפוץ, פותחו באופן טבעי עבור גלים רציפים (CW), ולכן אינן מותאמות ליישומים עם פולסים קצרים במיוחד ובפרט לפולסים בני מחזור בודד, הקריטיים לשליטה מדויקת במערכות מבוססות-גל. טכניקות מבוססות פאזה אלו סובלות לעיתים קרובות מ"אי-ודאות" בפאזה, מירידת איכות האות, ומעיוותים בזמן, דבר שמגביל את יעילותן הן בסימולציות והן בשימושים מעשיים.

מחקר זה מציע פתרון לאתגר הנ"ל באמצעות אלגוריתם חדש בשם Spatio-Temporal Adaptive Reconstruction (STAR), שפועל ישירות במישור הזמן, ומשולב עם גרסה כללית של שיטת הספקטרום הזוויתי (Generalized Angular Spectrum Method – GASM) לצורך תיאור מדויק של התפשטות סיגנלים רחבי סרט ובפרט פולסים קצרים. אף שהשיטה רלוונטית לתחומים כמו אופטיקה, אקוסטיקה ומכ"מים, יכולותיה מוצגות כאן בהקשר של אולטרה-סאונד רפואי. בהקשר זה, אלגוריתם STAR מאפשר עיצוב מדויק של אלומות לפולסים בני מחזור בודד ולתבניות מרובות-מוקדים, תוך התגברות על מגבלות של אלגוריתמים מסורתיים כמו GS ואף של גישות מבוססות למידה עמוקה.

מסגרת עבודה זו מאפשרת השגת רזולוציה משופרת, חלוקת אנרגיה מיטבית, והתאמה טובה יותר לעומקים ותדרים משתנים, כפי שאומת בסימולציות ובמדידות ניסיוניות. התוצאות מדגישות את הפוטנציאל של השיטה להשתלב במערכות זמן-אמת, ולסלול את הדרך להתקדמות משמעותית בהדמיית אולטרה-סאונד וביישומים מבוססי-גל נוספים.

אוניברסיטת תל אביב

הפקולטה להנדסה ע"ש איבי ואלדר פליישמן

בית הספר לתארים מתקדמים ע"ש זנדמן-סליינר

עיצוב אלומה של פולסים אולטרה-קצרים במישור הזמן לשימוש בדימות אולטרסאונד

חיבור זה הוגש כעבודת גמר לקראת התואר "מוסמך אוניברסיטה" בהנדסת חשמל

על-ידי

עוז שאול שאול

העבודה נעשתה בביה"ס להנדסת חשמל

בהנחיית פרופ' טלי אילוביץ